THE JOURNAL OF PHYSICAL CHEMISTRY A
A JOURNAL OF THE AMERICAN CHEMICAL SOCIETY

pubs.acs.org/JPCA Article

Commutator Matrix in Phase Space Mapping Models for Nonadiabatic Quantum Dynamics

Published as part of The Journal of Physical Chemistry virtual special issue "Yoshitaka Tanimura Festschrift".

Xin He, Baihua Wu, Zhihao Gong, and Jian Liu*

Cite This: *J. Phys. Chem. A* 2021, 125, 6845–6863 Read Online

ACCESS | Metrics & More | Article Recommendations | Supporting Information

ABSTRACT: We show that a novel, general phase space mapping Hamiltonian for nonadiabatic systems, which is reminiscent of the renowned Meyer–Miller mapping Hamiltonian, involves a commutator variable matrix rather than the conventional zero-point-energy parameter. In the exact mapping formulation on constraint space for phase space approaches for nonadiabatic dynamics, the general mapping Hamiltonian with commutator variables can be employed to generate approximate trajectory-based dynamics. Various benchmark model tests, which range from gas phase to condensed phase systems, suggest that the overall performance of the general mapping Hamiltonian is better than that of the conventional Meyer–Miller Hamiltonian.

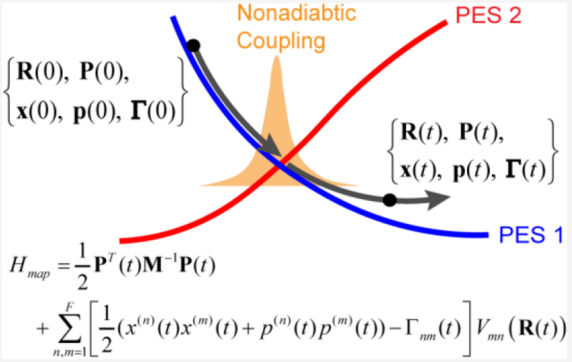

1. INTRODUCTION

Many important processes from photochemistry to electron transfer in chemical, biological, and materials systems involve quantum mechanical behavior of both electrons and nuclei in the context of nonadiabatic dynamics.[1−10] The celebrated Meyer–Miller mapping model[11−13] is one of the important theoretical frameworks for developing practical nonadiabatic dynamics methods.[14−56] Consider a coupled F-electronic-state Hamiltonian operator

$$\hat{H} = \sum_{n,m=1}^{F} H_{nm}(\hat{\mathbf{R}}, \hat{\mathbf{P}})|n\rangle\langle m| = \sum_{n,m=1}^{F}\left[\frac{1}{2}\hat{\mathbf{P}}^T\mathbf{M}^{-1}\hat{\mathbf{P}}\delta_{nm} + V_{nm}(\hat{\mathbf{R}})\right]|n\rangle\langle m| \quad (1)$$

in the diabatic representation (for simplicity), where the F electronic states consist of an orthogonal complete basis set, i.e.,

$$\langle m|n\rangle = \delta_{mn}$$
$$\hat{I}_{ele} = \sum_{n=1}^{F}|n\rangle\langle n|. \quad (2)$$

Here $\hat{I}_{ele}$ is the identity operator in the electronic state space, $\mathbf{M}$ is the diagonal "mass matrix" with elements $\{m_j\}$, $\{\mathbf{R},\mathbf{P}\}$ are the coordinate and momentum variables for the nuclear DOFs (with N the total number of nuclear DOFs), and potential energy elements $V_{nm}(\mathbf{R}) = V_{mn}(\mathbf{R})$ form a real symmetric matrix. The Meyer–Miller Hamiltonian reads

$$H_{\mathrm{MM}}(\mathbf{R}, \mathbf{P}; \mathbf{x}, \mathbf{p}) = \frac{1}{2}\mathbf{P}^T\mathbf{M}^{-1}\mathbf{P} + \sum_{n,m=1}^{F}\left[\frac{1}{2}(x^{(n)}x^{(m)} + p^{(n)}p^{(m)}) - \gamma\delta_{nm}\right]V_{nm}(\mathbf{R}) \quad (3)$$

where $\{\mathbf{x},\mathbf{p}\}=\{x^{(1)},\cdots,x^{(F)}, p^{(1)},\cdots,p^{(F)}\}$ are the mapping coordinate and momentum variables for the F electronic states.

There exist two alternative approaches that derive the Meyer–Miller mapping model in quantum mechanics.[12,13] The approach of Stock and Thoss[12] and of Sun et. al[14] suggests that parameter γ in the Meyer–Miller mapping Hamiltonian eq 3 is a parameter for the zero point energy of a singly excited oscillator for the underlying mapping DOFs for each electronic state,[30−33] which is in the similar spirit to that of the pioneering work of Meyer and Miller.[11] In comparison, the unified framework proposed in ref 13 offers a substantially different picture. It derives a mapping model reminiscent of the Meyer–Miller model,

Received: May 19, 2021
Revised: July 3, 2021
Published: August 2, 2021

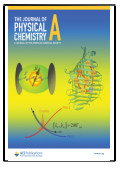

https://doi.org/10.1021/acs.jpca.1c04429
J. Phys. Chem. A 2021, 125, 6845–6863

$$H_{\mathrm{MM}}(\hat{\mathbf{R}}, \hat{\mathbf{P}}; \mathbf{x}, \mathbf{p}) = \sum_{n,m=1}^{F} \left[\frac{1}{2}(x^{(n)}x^{(m)} + p^{(n)}p^{(m)}) - \gamma\delta_{nm}\right] H_{mn}(\hat{\mathbf{R}}, \hat{\mathbf{P}}) \tag{4}$$

where parameter γ is interpreted as a parameter originated from a commutator of Pauli matrix $-\frac{i}{4}[\hat{\sigma}_x^{(n)}, \hat{\sigma}_y^{(n)}] = -\frac{\hat{\sigma}_z^{(n)}}{2}$, which allows both positive and negative values.[13,42] The one-to-one correspondence mapping formulation for the correlation function for nonadiabatic systems can rigorously be established.[41,42]

More interestingly, where the Meyer−Miller mapping Hamiltonian is rederived in the novel framework in ref 13, it is also indicated that there exists a more general mapping Hamiltonian

$$H_{map}(\mathbf{R}, \mathbf{P}; \mathbf{x}, \mathbf{p}; \mathbf{\Gamma}) = \sum_{n,m=1}^{F} \left[\frac{1}{2}(x^{(n)}x^{(m)} + p^{(n)}p^{(m)}) - \Gamma_{nm}\right] H_{mn}(\mathbf{R}, \mathbf{P}) \tag{5}$$

where $\mathbf{\Gamma}$ is a real symmetric matrix with the element Γ_{nm} in the nth row and mth column. Its element Γ_{nm} is a real variable for the corresponding commutator, $-\frac{i}{8}([\hat{\sigma}_x^{(n)}, \hat{\sigma}_y^{(m)}] + [\hat{\sigma}_x^{(m)}, \hat{\sigma}_y^{(n)}])$, as presented in ref 13. $\mathbf{\Gamma}$ is denoted the commutator matrix. When off-diagonal elements of commutator matrix $\mathbf{\Gamma}$ are set to zero and diagonal elements are the same, the general mapping Hamiltonian eq 5 is simplified to eq 4. Note that the commutator matrix $\mathbf{\Gamma}$ can evolve with time when eq 5 is utilized to generate corresponding Hamilton's equations of motion. To the best of our knowledge, except as presented in ref 13, the general mapping Hamiltonian eq 5 with commutator matrix $\mathbf{\Gamma}$ as a variable has *never* been proposed and used to generate the equations of motion for nonadiabatic dynamics. The purpose of the paper is to employ the general mapping Hamiltonian eq 5 for trajectory-based dynamics for nonadiabatic systems, in the exact mapping kernel formulation that we established in refs 41 and 42. The paper is organized as follows. Section 2 first reviews the one-to-one correspondence mapping formulation derived in refs 41 and 42 and then derives Hamilton's equations of motion from eq 5, where the frozen-nuclei limit as well as the Born−Oppenheimer limit are satisfied. Section 3 presents numerical results of various benchmark model tests for gas phase as well as condensed phase systems, which include the scattering models of Tully,[57] 3-state photodissociation models of Miller and coworkers,[58] 7-site model of the Fenna−Matthews−Olson (FMO) monomer,[59] and atom-in-cavity models.[60−63] Finally, conclusions are given in Section 4.

2. THEORY

2.1. Phase Space Mapping Formulations for Nonadiabatic Systems. Because it is convenient to obtain useful insight about the correspondence between quantum and classical concepts in phase space formulations of quantum mechanics,[64−82] they have been widely used in many areas of physics and chemistry since Wigner's pioneering work.[64] More recently, we have proposed a unified framework for the one-to-one correspondence mapping in phase space formulations of quantum mechanics,[42] which naturally includes and surpasses the classification scheme[79,81,82] for conventional approaches[64−78,80] for quantum systems represented in the continuous coordinate space and is able to treat quantum systems described in the finite-dimensional Hilbert space.[13,41] Such a framework offers a useful tool for nonadiabatic systems where both continuous nuclear degrees of freedom (DOFs) and discretized electronic state DOFs are involved.

In the unified framework of phase space mapping models for the (coupled) multistate Hamiltonian (eq 1) in ref 13, eq 4 is the mapping model reminiscent of the Meyer−Miller model. When the mapping variables for the electronic state DOFs satisfy

$$\sum_{n=1}^{F}\left[\frac{(x^{(n)})^2 + (p^{(n)})^2}{2} - \gamma\right] = 1 \tag{6}$$

the mapping Hamiltonian eq 4 is equal to the conventional Meyer−Miller Hamiltonian eq 3. This was first proposed in ref 41 for general F-state systems. The simplest way is to use the full constraint electronic space that eq 6 defines, i.e.,

$$\mathcal{S}(\mathbf{x}, \mathbf{p}): \delta\left(\sum_{n=1}^{F}\left[\frac{(x^{(n)})^2 + (p^{(n)})^2}{2}\right] - (1 + F\gamma)\right) \tag{7}$$

for constructing the formulation for physical properties in the mapping approach. The possible value of parameter γ for eq 6 or eq 7 implies $\gamma \in (-\frac{1}{F}, \infty)$.

The trace of a product of two operators is expressed in phase space as

$$\mathrm{Tr}_{n,e}[\hat{A}\hat{B}] = \int (2\pi\hbar)^{-N} \mathrm{d}\mathbf{R}\, \mathrm{d}\mathbf{P} \int_{\mathcal{S}(\mathbf{x},\mathbf{p})} F\, \mathrm{d}\mathbf{x}\, \mathrm{d}\mathbf{p} \times A(\mathbf{R}, \mathbf{P}; \mathbf{x}, \mathbf{p})\tilde{B}(\mathbf{R}, \mathbf{P}; \mathbf{x}, \mathbf{p}) \tag{8}$$

where

$$A(\mathbf{R}, \mathbf{P}; \mathbf{x}, \mathbf{p}) = \mathrm{Tr}_{n,e}[\hat{A}\hat{K}_{nuc}(\mathbf{R}, \mathbf{P}) \otimes \hat{K}_{ele}(\mathbf{x}, \mathbf{p})] \tag{9}$$

$$\tilde{B}(\mathbf{R}, \mathbf{P}; \mathbf{x}, \mathbf{p}) = \mathrm{Tr}_{n,e}[\hat{K}_{nuc}^{-1}(\mathbf{R}, \mathbf{P}) \otimes \hat{K}_{ele}^{-1}(\mathbf{x}, \mathbf{p})\hat{B}] \tag{10}$$

$(2\pi\hbar)^{-N}\, \mathrm{d}\mathbf{R}\, \mathrm{d}\mathbf{P} \otimes F\, \mathrm{d}\mathbf{x}\, \mathrm{d}\mathbf{P}$ stands for the invariant measure on the mapping phase space for nuclear and electronic state DOFs, and Tr_n and Tr_e represent the trace over the nuclear DOFs and that over the F electronic states, respectively. The mapping kernel and its inverse satisfy the normalization

$$\mathrm{Tr}_n[\hat{K}_{nuc}(\mathbf{R}, \mathbf{P})] = \mathrm{Tr}_n[\hat{K}_{nuc}^{-1}(\mathbf{R}, \mathbf{P})] = 1$$
$$\mathrm{Tr}_e[\hat{K}_{ele}(\mathbf{x}, \mathbf{p})] = \mathrm{Tr}_e[\hat{K}_{ele}^{-1}(\mathbf{x}, \mathbf{p})] = 1 \tag{11}$$

and

$$(2\pi\hbar)^{-N}\int \mathrm{d}\mathbf{R}\, \mathrm{d}\mathbf{P}\, \hat{K}_{nuc}(\mathbf{R}, \mathbf{P}) = \hat{I}_{nuc}$$
$$(2\pi\hbar)^{-N}\int \mathrm{d}\mathbf{R}\, \mathrm{d}\mathbf{P}\, \hat{K}_{nuc}^{-1}(\mathbf{R}, \mathbf{P}) = \hat{I}_{nuc}$$
$$\int_{\mathcal{S}(\mathbf{x},\mathbf{p})} F\, \mathrm{d}\mathbf{x}\, \mathrm{d}\mathbf{p}\, \hat{K}_{ele}(\mathbf{x}, \mathbf{p}) = \hat{I}_{ele}$$
$$\int_{\mathcal{S}(\mathbf{x},\mathbf{p})} F\, \mathrm{d}\mathbf{x}\, \mathrm{d}\mathbf{p}\, \hat{K}_{ele}^{-1}(\mathbf{x}, \mathbf{p}) = \hat{I}_{ele} \tag{12}$$

where $\hat{I}_{nuc}$ is the identity operator in the nuclear space and the integral over constraint mapping space $\mathcal{S}(\mathbf{x}, \mathbf{p})$ is

https://doi.org/10.1021/acs.jpca.1c04429
J. Phys. Chem. A 2021, 125, 6845−6863

$$\int_{S(\mathbf{x},\mathbf{p})} F\, d\mathbf{x}\, d\mathbf{p}\, g(\mathbf{x},\mathbf{p}) = \frac{\int F\, d\mathbf{x}\, d\mathbf{p}\, \delta\left(\sum_{n=1}^{F}\left[\frac{(x^{(n)})^2+(p^{(n)})^2}{2}\right]-(1+F\gamma)\right) g(\mathbf{x},\mathbf{p})}{\int d\mathbf{x}\, d\mathbf{p}\, \delta\left(\sum_{n=1}^{F}\left[\frac{(x^{(n)})^2+(p^{(n)})^2}{2}\right]-(1+F\gamma)\right)} \tag{13}$$

The one-to-one correspondence mapping from $A(\mathbf{R},\mathbf{P};\mathbf{x},\mathbf{p})$ (or $\tilde{B}(\mathbf{R},\mathbf{P};\mathbf{x},\mathbf{p})$) of eq 9 back to operator $\hat{A}$ (or $\hat{B}$) is

$$\hat{A} = \int (2\pi\hbar)^{-N} d\mathbf{R}\, d\mathbf{P} \int_{S(\mathbf{x},\mathbf{p})} F\, d\mathbf{x}\, d\mathbf{p}\; A(\mathbf{R},\mathbf{P};\mathbf{x},\mathbf{p})\hat{K}_{nuc}^{-1}(\mathbf{R},\mathbf{P}) \otimes \hat{K}_{ele}^{-1}(\mathbf{x},\mathbf{p})$$
$$\hat{B} = \int (2\pi\hbar)^{-N} d\mathbf{R}\, d\mathbf{P} \int_{S(\mathbf{x},\mathbf{p})} F\, d\mathbf{x}\, d\mathbf{p}\; \tilde{B}(\mathbf{R},\mathbf{P};\mathbf{x},\mathbf{p})\hat{K}_{nuc}(\mathbf{R},\mathbf{P}) \otimes \hat{K}_{ele}(\mathbf{x},\mathbf{p}). \tag{14}$$

The mapping kernel for the nuclear DOFs (in eq 9) is

$$\hat{K}_{nuc}(\mathbf{R},\mathbf{P}) = \left(\frac{\hbar}{2\pi}\right)^N \int d\boldsymbol{\zeta} \int d\boldsymbol{\eta}\; e^{i\boldsymbol{\zeta}\cdot(\hat{\mathbf{R}}-\mathbf{R})+i\boldsymbol{\eta}\cdot(\hat{\mathbf{P}}-\mathbf{P})} f(\boldsymbol{\zeta},\boldsymbol{\eta}) \tag{15}$$

and its inverse is

$$\hat{K}_{nuc}^{-1}(\mathbf{R},\mathbf{P}) = \left(\frac{\hbar}{2\pi}\right)^N \int d\boldsymbol{\zeta} \int d\boldsymbol{\eta}\; e^{-i\boldsymbol{\zeta}\cdot(\hat{\mathbf{R}}-\mathbf{R})-i\boldsymbol{\eta}\cdot(\hat{\mathbf{P}}-\mathbf{P})} [f(-\boldsymbol{\zeta},-\boldsymbol{\eta})]^{-1} \tag{16}$$

where $f(\boldsymbol{\zeta},\boldsymbol{\eta})$ is a scalar function to determine the corresponding nuclear phase space. For instance, the Wigner function[64,65] has

$$f(\boldsymbol{\zeta},\boldsymbol{\eta}) = 1 \tag{17}$$

and the Husimi function[68] has

$$f(\boldsymbol{\zeta},\boldsymbol{\eta}) = \exp\left(-\frac{\boldsymbol{\zeta}^T\mathbf{G}^{-1}\boldsymbol{\zeta}}{4} - \frac{\hbar^2}{4}\boldsymbol{\eta}^T\mathbf{G}\boldsymbol{\eta}\right) \tag{18}$$

The mapping kernel for the F electronic states (in eq 9) is

$$\hat{K}_{ele}(\mathbf{x},\mathbf{p}) = \sum_{n,m=1}^{F}\left[\frac{1}{2}(x^{(n)}+ip^{(n)})(x^{(m)}-ip^{(m)}) - \gamma\delta_{nm}\right]|n\rangle\langle m| \tag{19}$$

and the inverse kernel

$$\hat{K}_{ele}^{-1}(\mathbf{x},\mathbf{p}) = \sum_{n,m=1}^{F}\left[\frac{1+F}{2(1+F\gamma)^2}(x^{(n)}+ip^{(n)}) \times (x^{(m)}-ip^{(m)}) - \frac{1-\gamma}{1+F\gamma}\delta_{nm}\right]|n\rangle\langle m| \tag{20}$$

In eqs 8, 12, 14, 15, and 16, while the integrals for the nuclear DOFs are over the whole nuclear phase space when the Wigner or Husimi function is employed, those for the F electronic states are over the constraint electronic mapping space, $\mathcal{S}(\mathbf{x},\mathbf{p})$.

When the nuclear DOFs are described in Wigner phase space (eqs 15 and 16 with eq 17), the mapping kernel and its inverse are the same, i.e.,

$$\hat{K}_{nuc}(\mathbf{R},\mathbf{P}) = \hat{K}_{nuc}^{-1}(\mathbf{R},\mathbf{P}) \tag{21}$$

When the Wigner function (eqs 15 and 16 with eq 17) is used for the nuclear DOFs, it is easy to show that the real part of the mapping Hamiltonian $H(\mathbf{R},\mathbf{P};\mathbf{x},\mathbf{p}) = \mathrm{Tr}_{n,e}[\hat{H}\hat{K}_{nuc}(\mathbf{R},\mathbf{P}) \otimes \hat{K}_{ele}(\mathbf{x},\mathbf{p})]$ with constraint eq 7 for the coupled multistate Hamiltonian operator eq 1 is the same as the conventional Meyer−Miller Hamiltonian eq 3. The equations of motion produced by the real part of $H(\mathbf{R},\mathbf{P};\mathbf{x},\mathbf{p}) = \mathrm{Tr}_{n,e}[\hat{H}\hat{K}_{nuc}(\mathbf{R},\mathbf{P}) \otimes \hat{K}_{ele}(\mathbf{x},\mathbf{p})]$ are identical with those yielded by its imaginary part.

When the parameter

$$\gamma = \frac{\sqrt{F+1}-1}{F} \tag{22}$$

is employed, the mapping kernel for the electronic DOFs is equal to the inverse kernel, i.e.,

$$\hat{K}_{ele}(\mathbf{x},\mathbf{p}) = \hat{K}_{ele}^{-1}(\mathbf{x},\mathbf{p}) \tag{23}$$

eq 22 offers the only physical value for parameter γ in the region $(-\frac{1}{F}, \infty)$ to make eq 23 hold. We note that the so-called spin mapping model of refs 43 and 44 intrinsically based on the Meyer−Miller mapping Hamiltonian model (especially when $F \geq 3$ electronic states are involved) is only a special case of the exact phase space mapping formulation that we established first in refs 13 and 41 and then in ref 42, i.e., parameter $\gamma = 0$, $(\sqrt{F+1}-1)/F$, or 1 in our exact phase space mapping formulation corresponds to the Q-version, W-version, or P-version of refs 43 and 44, respectively. Interestingly, the authors of ref 44 even failed to understand that the interpretation for general F-state systems constructed in Appendix A of ref 41 is simply an exact phase space mapping formulation for the parameter $\gamma = 0$. We also note that the exact phase space mapping formulation of the correlation function can be used to formalize various other methods based on the Meyer−Miller mapping Hamiltonian model in refs 14, 35, 45, 46, 49, and 83−86, as we will show in a forthcoming paper.

2.2. Expression of the Time Correlation Function. Define the Heisenberg operator $\hat{B}(t) = e^{iHt/\hbar}\hat{B}e^{-itHt/\hbar}$. As a result of eq 8, an exact expression of the time correlation function of the nonadiabatic system

$$C_{AB}(t) = \mathrm{Tr}_{n,e}[\hat{A}(0)\hat{B}(t)] \tag{24}$$

is

$$C_{AB}(t) = \int (2\pi\hbar)^{-N} d\mathbf{R}\, d\mathbf{P} \int_{S(\mathbf{x},\mathbf{p})} F\, d\mathbf{x}\, d\mathbf{p}\; \times A(\mathbf{R},\mathbf{P};\mathbf{x},\mathbf{p})\tilde{B}(\mathbf{R},\mathbf{P};\mathbf{x},\mathbf{p};t) \tag{25}$$

where

$$\tilde{B}(\mathbf{R},\mathbf{P};\mathbf{x},\mathbf{p};t) = \mathrm{Tr}_{n,e}[\hat{K}_{nuc}^{-1}(\mathbf{R},\mathbf{P}) \otimes \hat{K}_{ele}^{-1}(\mathbf{x},\mathbf{p})\hat{B}(t)] \tag{26}$$

When nuclear and electronic dynamics is exactly solved in eq 26, the correlation function formulation eq 25 is exact for nonadiabatic systems.[41,42]

When trajectory-based dynamics is introduced, eq 25 is recast into

$$C_{AB}(t) = \int (2\pi\hbar)^{-N} d\mathbf{R}\, d\mathbf{P} \int_{S(\mathbf{x},\mathbf{p})} F\, d\mathbf{x}\, d\mathbf{p}\; \times A(\mathbf{R},\mathbf{P};\mathbf{x},\mathbf{p})\tilde{B}(\mathbf{R}_t,\mathbf{P}_t;\mathbf{x}_t,\mathbf{p}_t) \tag{27}$$

https://doi.org/10.1021/acs.jpca.1c04429
J. Phys. Chem. A 2021, 125, 6845−6863

In the frozen-nuclei limit where only the electronic DOFs are involved (i.e., nuclear coordinate $\mathbf{R}$ and nuclear momentum $\mathbf{P}$ are fixed), Hamilton's equations of motion from the Meyer–Miller Hamiltonian eq 3 lead to exact results. When both nuclear and electronic DOFs are considered, exact equations of motion for the trajectories are far from trivial to solve numerically. When the independent trajectory is introduced to eq 27, it is then often an approximation to eq 25. For instance, when the Meyer–Miller Hamiltonian, eq 3, is used to generate the independent trajectory for both nuclear and electronic DOFs in eq 27, it is equivalent to the extended classical mapping model (eCMM) approach[41,42] where the linearized semiclassical or linearized path integral approximation[14,87,88] is utilized for only the nuclear DOFs.

Note that the one-to-one correspondence mapping framework for eq 8 as well as eq 25 only depends on the constraint phase space defined by eq 7. That is, the exact mapping framework is intrinsically *independent* of the form of the mapping Hamiltonian for dynamics. The Meyer–Miller Hamiltonian, eq 3, is not necessary to be the *only* choice for yielding the equations of motion for the independent trajectory for eq 27. The derivation procedure for eq 43 for Model II of ref 13 suggests that a more comprehensive form for the phase space mapping Hamiltonian model is eq 5. When the equality

$$\sum_{n=1}^{F}\left[\frac{(x^{(n)})^2+(p^{(n)})^2}{2}-\Gamma_{nn}\right]=1 \tag{28}$$

holds, eq 5 becomes

$$H_{map}(\mathbf{R},\mathbf{P};\mathbf{x},\mathbf{p};\boldsymbol{\Gamma})=\frac{1}{2}\mathbf{P}^T\mathbf{M}^{-1}\mathbf{P}+\sum_{n,m=1}^{F}\left[\frac{1}{2}(x^{(n)}x^{(m)}+p^{(n)}p^{(m)})-\Gamma_{nm}\right]V_{mn}(\mathbf{R}) \tag{29}$$

Any Hermitian matrix $\boldsymbol{\Gamma}$ can be represented by its eigenvalues $\{\lambda_k\}$ and eigenvectors $\{\mathbf{b}_k\}$, i.e.,

$$\boldsymbol{\Gamma}=\sum_{k=1}^{F}\lambda_k\mathbf{b}_k\mathbf{b}_k^{\dagger} \tag{30}$$

with $\boldsymbol{\Gamma}\mathbf{b}_k=\lambda_k\,\mathbf{b}_k$ and symbol † standing for the complex conjugate transpose. As its eigenvalues $\{\lambda_k\}$ are real, define $\mathbf{c}_k=|\lambda_k|^{1/2}\mathbf{b}_k$, and eq 30 can be recast into

$$\boldsymbol{\Gamma}=\sum_{k=1}^{F}s_k\mathbf{c}_k\mathbf{c}_k^{\dagger} \tag{31}$$

Here, parameter

$$s_k=\mathrm{sgn}(\lambda_k) \tag{32}$$

is the sign of the eigenvalue λ_k. Using

$$c_k^{(n)}=(\tilde{x}_k^{(n)}+i\tilde{p}_k^{(n)})/\sqrt{2} \tag{33}$$

to represent the nth element of vector $\mathbf{c}_k$, we obtain

$$\Gamma_{nm}=\sum_{k=1}^{F}\frac{s_k}{2}(\tilde{x}_k^{(n)}+i\tilde{p}_k^{(n)})(\tilde{x}_k^{(m)}-i\tilde{p}_k^{(m)}) \tag{34}$$

Here, $\tilde{x}_k^{(n)}$ and $\tilde{p}_k^{(n)}$ are two real auxiliary variables. Because the commutator matrix of eq 29 is a real symmetric matrix, eq 34 is simplified to

$$\Gamma_{nm}=\sum_{k=1}^{F}\frac{s_k}{2}(\tilde{x}_k^{(n)}\tilde{x}_k^{(m)}+\tilde{p}_k^{(n)}\tilde{p}_k^{(m)}) \tag{35}$$

The mapping Hamiltonian eq 29 then becomes

$$H_{map}(\mathbf{R},\mathbf{P};\mathbf{x},\mathbf{p};\tilde{\mathbf{x}},\tilde{\mathbf{p}})=\frac{1}{2}\mathbf{P}^T\mathbf{M}^{-1}\mathbf{P}+\sum_{n,m=1}^{F}V_{mn}(\mathbf{R})\left[\frac{1}{2}(x^{(n)}x^{(m)}+p^{(n)}p^{(m)})-\sum_{k=1}^{F}\frac{s_k}{2}(\tilde{x}_k^{(n)}\tilde{x}_k^{(m)}+\tilde{p}_k^{(n)}\tilde{p}_k^{(m)})\right] \tag{36}$$

The equations of motion governed by eq 36 are

$$\dot{\mathbf{R}}=\mathbf{M}^{-1}\mathbf{P}$$

$$\dot{\mathbf{P}}=-\sum_{n,m=1}^{F}\frac{\partial V_{mn}(\mathbf{R})}{\partial\mathbf{R}}\left[\frac{1}{2}(x^{(n)}x^{(m)}+p^{(n)}p^{(m)})-\sum_{k=1}^{F}\frac{s_k}{2}(\tilde{x}_k^{(n)}\tilde{x}_k^{(m)}+\tilde{p}_k^{(n)}\tilde{p}_k^{(m)})\right] \tag{37}$$

for nuclear DOFs, and

$$\dot{x}^{(n)}=\sum_{m=1}^{F}V_{nm}(\mathbf{R})p^{(m)}$$

$$\dot{p}^{(n)}=-\sum_{m=1}^{F}V_{nm}(\mathbf{R})x^{(m)}$$

$$\dot{\tilde{x}}_k^{(n)}=-s_k\sum_{m=1}^{F}V_{nm}(\mathbf{R})\tilde{p}_k^{(m)}$$

$$\dot{\tilde{p}}_k^{(n)}=s_k\sum_{m=1}^{F}V_{nm}(\mathbf{R})\tilde{x}_k^{(m)}. \tag{38}$$

for the electronic mapping DOFs $\{\mathbf{x},\mathbf{p}\}$ and auxiliary variables $\{\tilde{\mathbf{x}},\tilde{\mathbf{p}}\}$ for the commutator matrix. We denote this scheme the extended classical mapping model with commutator variables (eCMMcv). Because eq 28 holds at the beginning, it is straightforward to verify that the equations of motion (eqs 37 and 38) generated from the mapping Hamiltonian (eq 36) conserve the two properties,

$$\sum_{n=1}^{F}\left[\frac{(x^{(n)})^2+(p^{(n)})^2}{2}\right]=(1+F\gamma) \tag{39}$$

This is equivalent to eq 7, and

$$\sum_{n,k=1}^{F}\frac{s_k}{2}((\tilde{x}_k^{(n)})^2+(\tilde{p}_k^{(n)})^2)=F\gamma \tag{40}$$

Because eq 39 holds, the exact mapping framework for eq 8 as well as eq 25 for the electronic DOFs is still valid.

Further consider that the initial electronic state is localized at state $|j_{occ}\rangle$. While the initial condition for $(\mathbf{x},\mathbf{p})$ is uniformly sampled on constraint space $\mathcal{S}(\mathbf{x},\mathbf{p})$ that depicts the mapping framework for the electronic DOFs, the initial condition for auxiliary variables $\{\tilde{\mathbf{x}},\tilde{\mathbf{p}}\}$ for commutator matrix Γ is given by

https://doi.org/10.1021/acs.jpca.1c04429
J. Phys. Chem. A 2021, 125, 6845−6863

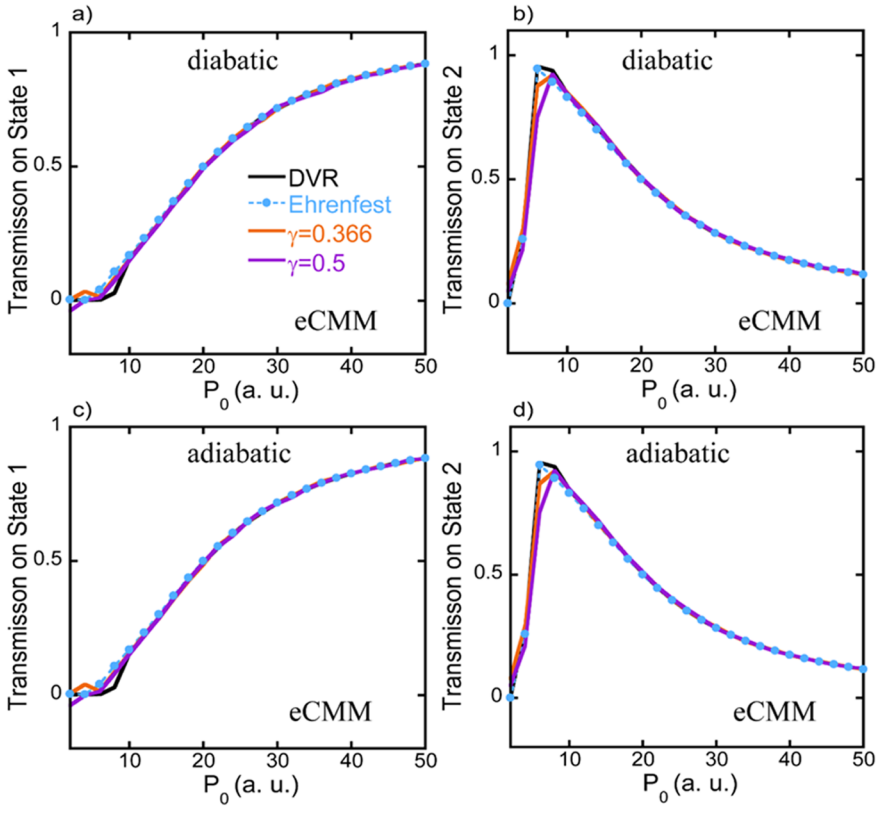

Figure 1. Transmission coefficients of Tully's SAC model. In panel a, range and purple solid lines: The eCMM transmission coefficients on state 1 for $\gamma = 0.366$ and $\gamma = 0.5$, respectively. Black solid line: Exact results yielded by DVR. Blue dashed line with circles: Ehrenfest dynamics. Panel b is similar to Panel a but for the eCMM transmission coefficients on state 2. Panels c and d are the same as panels a and b, respectively, except that the adiabatic representation is used in panels c and d. The transmission coefficients in the adiabatic representation are transformed to those in the diabatic representation for fair comparison.

$$\frac{s_k}{2}((\tilde{x}_k^{(n)}(0))^2 + (\tilde{p}_k^{(n)}(0))^2) = \left[\frac{(x^{(n)}(0))^2 + (p^{(n)}(0))^2}{2} - \delta_{n,j_{occ}}\right]\delta_{nk} \tag{41}$$

with

$$s_k = \begin{cases} -1 \text{ when} \dfrac{(x^{(k)}(0))^2 + (p^{(k)}(0))^2}{2} < 1 \text{ and } k = j_{occ} \\ 1 \text{ elsewhere} \end{cases} \tag{42}$$

such that the equations of motion of eqs 37and 38 approach the Born−Oppenheimer limit for each trajectory when state−state coupling terms $\{V_{nm}(\mathbf{R})\}$ vanish for all $n \neq m$; i.e., it yields

$$\left[\frac{1}{2}((x^{(n)})^2 + (p^{(n)})^2) - \sum_{k=1}^{F}\frac{s_k}{2}((\tilde{x}_k^{(n)})^2 + (\tilde{p}_k^{(n)})^2)\right] = \delta_{n,j_{occ}} \tag{43}$$

The strategy similar to eq 43 has already been used in a few approaches based on the Meyer−Miller mapping Hamiltonian.[29,89,90] Because eqs 41 and 42 satisfy eq 28, the comprehensive phase space mapping Hamiltonian proposed by eq 5 is identical with eq 29 as well as eq 36. Then, eq 41 defines the constraint space for the initial conditions for auxiliary variables $\{\tilde{\mathbf{x}},\tilde{\mathbf{p}}\}$ for commutator matrix $\mathbf{\Gamma}$,

$$\xi(\tilde{\mathbf{x}}(0), \tilde{\mathbf{p}}(0)): \prod_{k,n=1}^{F}\delta\left(\frac{s_k}{2}((\tilde{x}_k^{(n)}(0))^2 + (\tilde{p}_k^{(n)}(0))^2) - \left[\frac{(x^{(n)}(0))^2 + (p^{(n)}(0))^2}{2} - \delta_{n,j_{occ}}\right]\delta_{nk}\right) \tag{44}$$

When the initial values for $(\mathbf{R},\mathbf{P};\mathbf{x},\mathbf{p})$ are the same, any point on constraint space $\xi\{\tilde{\mathbf{x}},\tilde{\mathbf{p}}\}$ as the initial values for auxiliary variables $\{\tilde{\mathbf{x}},\tilde{\mathbf{p}}\}$ for matrix $\mathbf{\Gamma}$ leads to the same values for $(\mathbf{R}_t,\mathbf{P}_t;\mathbf{x}_t,\mathbf{p}_t)$ at time t along the trajectory yielded by the equations of motion, eqs 37 and 38. Note that only the initial values for $(\mathbf{R},\mathbf{P};\mathbf{x},\mathbf{p})$ and the values for $(\mathbf{R}_t, \mathbf{P}_t; \mathbf{x}_t, \mathbf{p}_t)$ at time t are employed in the correlation function, eq 27. Once that the initial values for physical variables $(\mathbf{R}, \mathbf{P}; \mathbf{x}, \mathbf{p})$ are given, we only choose a specific point on constraint space $\xi\{\tilde{\mathbf{x}}, \tilde{\mathbf{p}}\}$ as the initial values for auxiliary variables $\{\tilde{\mathbf{x}}, \tilde{\mathbf{p}}\}$, because it is *not* necessary to do sampling on constraint space $\xi\{\tilde{\mathbf{x}}, \tilde{\mathbf{p}}\}$. It is easy to prove that the equations of motion of eqs 37 and 38 also approach the frozen-nuclei limit when only the electronic DOFs are involved (i.e., nuclear coordinate $\mathbf{R}$ and nuclear momentum $\mathbf{P}$ are fixed). That is, eq 35 is equivalent to solving the time-dependent Schrödinger equation for the electronic DOFs when the nuclear DOFs are frozen. A more convenient and equivalent way to evolve electronic maping DOFs and auxiliary variables in eCMMcv is to treat them in the matrix representation, which is provided in Section S1-A of the Supporting Information.

https://doi.org/10.1021/acs.jpca.1c04429
J. Phys. Chem. A 2021, 125, 6845−6863

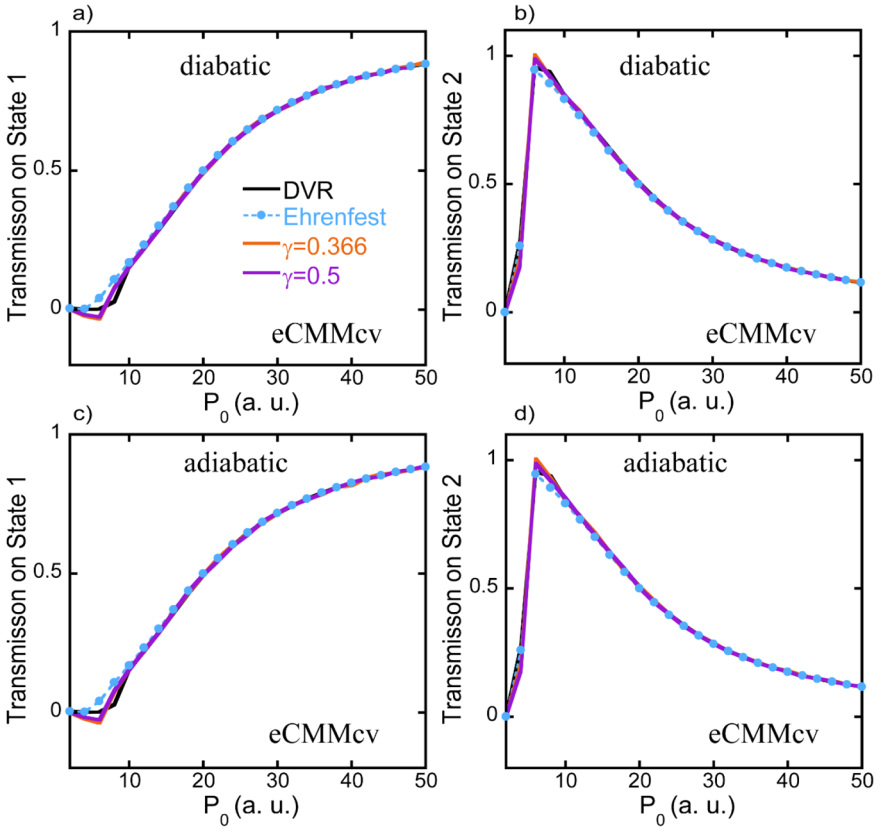

Figure 2. Same as Figure 1, but for transmission coefficients obtained by eCMMcv.

In summary, the expression of the correlation function eq 27 on constraint space $\mathcal{S}(\mathbf{x}, \mathbf{p})$ for the electronic DOFs and Wigner phase space for the nuclear DOFs, trajectory-based dynamics (eqs 37 and 38) governed by the general mapping Hamiltonian eq 36, and initial values for auxiliary variables $\{\tilde{\mathbf{x}}, \tilde{\mathbf{p}}\}$ defined by a point on constraint space $\xi\{\tilde{\mathbf{x}}, \tilde{\mathbf{p}}\}$ are all necessary elements for eCMMcv, the phase space mapping approach for nonadiabatic dynamics which we propose in this paper. The eCMMcv approach meets the frozen-nuclei limit as well as the Born−Oppenheimer limit.

Finally, it is straightforward to express eCMMcv (or eCMM) in the adiabatic representation or other representations. When the general mapping Hamiltonian with the commutator matrix is used in eCMMcv to yield the equations of motion, they are similar to the equations of motion generated by the Meyer−Miller Hamiltonian. The strategy of Cotton and Miller in ref 26 can directly be extended to the general mapping Hamiltonian in the adiabatic representation. (See Section S1 of Supporting Information for more discussion.)

3. RESULTS AND DISCUSSIONS

Below we test the numerical performance of eCMMcv for a few illustrative benchmark gas phase and condensed phase systems. We first apply eCMMcv to Tully's scattering models[57] that contain single avoided crossing (SAC) and dual avoided crossing (DAC) examples. The second application consists of photodissociation models of Miller and co-workers,[58] where more realistic Morse potentials are involved. We then test typical system−bath models for condensed phase dissipative systems,[91] which include the 7-state Fenna−Matthews−Olson (FMO) monomer that appears in photosynthesis in green sulfur bacteria[59,92] and strongly coupled optical cavity-molecular matter systems used to control and manipulate chemical and physical processes.[50,60−63,93]

3.1. Tully's Scattering Models. Tully's scattering models[57] are often used as benchmark applications to test nonadiabatic dynamics methods. The SAC and DAC models that mimic the surface intersection in molecular systems have widely been tested for mapping model dynamics.[18,21,49,94]

Tully's scattering problems are described by a two-state Hamiltonian (with the form of eq 1) with an atom of mass m = 2000 au After scattering in the interaction region, the system evolves in plateau regions where diabatic potential functions $V_m(R \to \infty)$ and $V_m(R \to -\infty)$ are flat. The transmission and reflection coefficients are calculated for state n. In each eCMM or eCMMcv simulation, fully converged results are obtained by an ensemble average over 96 000 trajectories.

3.1.1. Single Avoided Crossing. In the SAC model, the diagonal elements of the potential operator are $V_{11} = -V_{22} = A(1 - e^{-B|R|})\mathrm{sgn}(R)$ and off-diagonal ones are $V_{12} = V_{21} = Ce^{-DR^2}$. The parameters (using atomic units) are A = 0.01, B = 1.6, C = 0.005, and D = 1.0. The initial condition follows an occupation on the state 1 with the initial nuclear wavepacket $\Psi(R;t = 0) \propto \exp[-\alpha(R - R_0)^2/2 + i\,(R - R_0)P_0/\hbar]$, where the Gaussian width parameter is α = 1 au, the initial average coordinate is R_0 = −3.8 au, and the initial average momentum is P_0. The initial Wigner distribution for the nuclear coordinate is then $\rho_W^{\mathrm{nuc}}(R, P) \propto \exp[-\alpha(R - R_0)^2 - (P - P_0)^2/(\alpha\hbar^2)]$.

In the simulations the initial average momentum P_0 ranges from 2 to 50 au. We present numerical results for the transmission coefficients in Figure 1 and Figure 2. While panels a and b of Figure 1 demonstrate the transmission coefficient of

https://doi.org/10.1021/acs.jpca.1c04429
J. Phys. Chem. A 2021, 125, 6845−6863

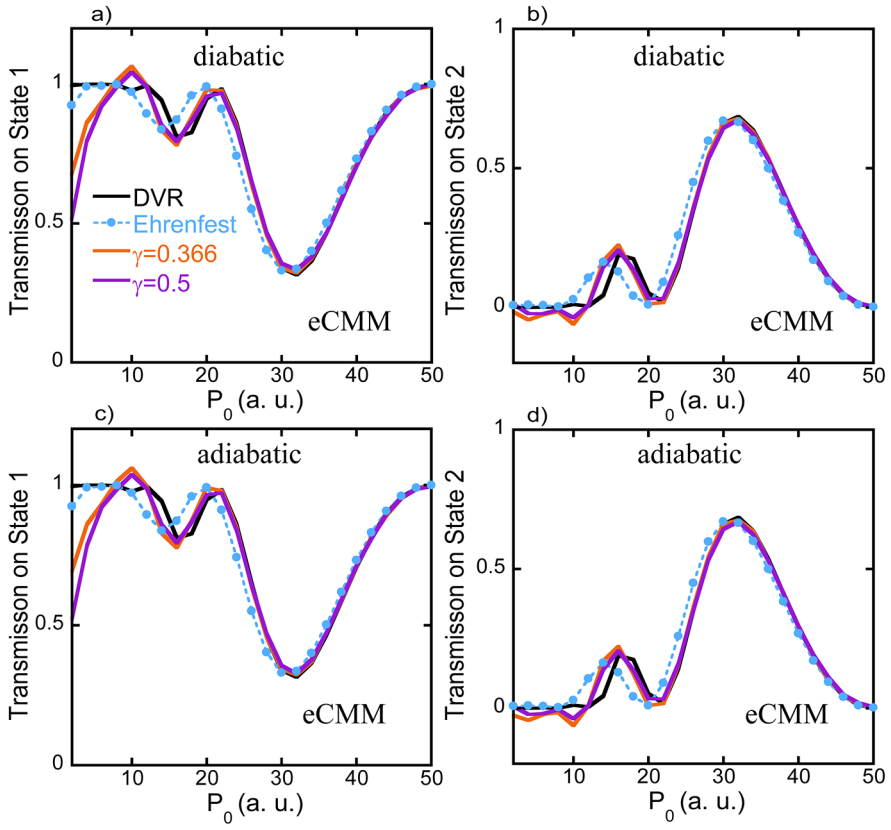

Figure 3. Transmission coefficients of Tully's DAC model. In panel a, orange and purple solid lines: eCMM transmission coefficients on state 1 for γ = 0.366 and γ = 0.5, respectively. Black solid line: Exact results yielded by DVR. Blue dashed line with circles: Ehrenfest dynamics. Panel b is similar to panel a but for the eCMM transmission coefficients on state 2. Panels c and d are the same as panels a and b, respectively, except that the adiabatic representation is used in panels c and d. The transmission coefficients in the adiabatic representation are transformed to those in the diabatic representation for fair comparison.

state 1 and that of state 2, respectively, for eCMM in the diabatic representation, panels c and d of Figure 1 show those calculated by eCMM in the adiabatic representation. Figure 2 then presents those results obtained by eCMMcv. Two values $\gamma = (\sqrt{F+1} - 1)/F = 0.366$ and $\gamma = {}^1/_2$ are used for parameter γ in eq 7 for eCMM and that in eq 39 for eCMMcv. Figures 1 and 2 demonstrate that either eCMM or eCMMcv yields results close to the exact transmission of either of state 1 and state 2 in a large range of the initial average momentum ($P_0 \geq 10$ au), independent of the choice of γ and of the representation of the electronic states. In the small initial average momentum region ($P_0 < 10$ au), the exact results produced by the discrete variable representation (DVR) approach[95] exhibit a threshold. Both eCMM and eCMMcv are competent in capturing such a threshold. Comparison between eCMM (Figure 1) and eCMMcv (Figure 2) shows that eCMMcv is less sensitive to the value of parameter γ. (More comparison is available in Section S2 of the Supporting Information.) The regime $[(\sqrt{F+1} - 1)/F, 1/2]$ is recommended for γ in eCMMcv. We then focus on this reasonable regime for parameter γ, which will be tested for the rest of the benchmark models in the paper.

3.1.2. Dual Avoided Crossing. In the DAC model, the diagonal elements of the potential operator are $V_{11} = 0$ and $V_{22} = -Ae^{-BR^2} + E_0$, and the off-diagonal ones are $V_{12} = V_{21} = Ce^{-DR^2}$, where the parameters are set as $A = 0.10$, $B = 0.28$, $E_0 = 0.05$, $C = 0.015$, and $D = 0.06$. Two crossing points appear in the diagonal potential energy surfaces. At time $t = 0$, state 1 is occupied with the initial nuclear wavepacket $\Psi(R;t=0) \propto \exp[-\alpha(R-R_0)^2/2 + i(R-R_0)P_0/\hbar]$, where the Gaussian width parameter is $\alpha = 1$ au, the initial average coordinate is $R_0 = -10$ au, and the initial average momentum P_0 varies from 2 to 50 au.

Results for the transmission coefficients are presented in Figure 3 and Figure 4. Panels a and b in Figure 3 show the eCMM results on state 1 and on state 2, respectively, using the diabatic representation. The results produced by Ehrenfest (mean field) dynamics demonstrate a noticeable deviation from the exact DVR data for $P_0 \geq 10$ au. The eCMM approach with either $\gamma = (\sqrt{F+1} - 1)/F = 0.366$ or $\gamma = {}^1/_2$ yields accurate results for the relatively large initial average momentum ($P_0 \geq 10$ au). It captures the correct shape of Stückelberg oscillations.[14,57,96] The eCMM results calculated in the adiabatic representation shown in panels c and d of Figure 3 are consistent with those in the diabatic representation demonstrated in Panels 3(a) and 3(b). Figure 4 presents the eCMMcv results for the same model. In comparison to the eCMM results of Figure 3, the eCMMcv data of Figure 4 show better performance in a large range of initial average momentum and are also less sensitive to parameter γ.

3.2. Three-State Photodissociation Models of Miller and Co-workers. The coupled three states with Morse oscillators proposed by Miller and co-workers,[58] which mimic ultrafast photodissociation processes, provide another set of gas phase benchmark models for testing nonadiabatic dynamics

https://doi.org/10.1021/acs.jpca.1c04429
J. Phys. Chem. A 2021, 125, 6845−6863

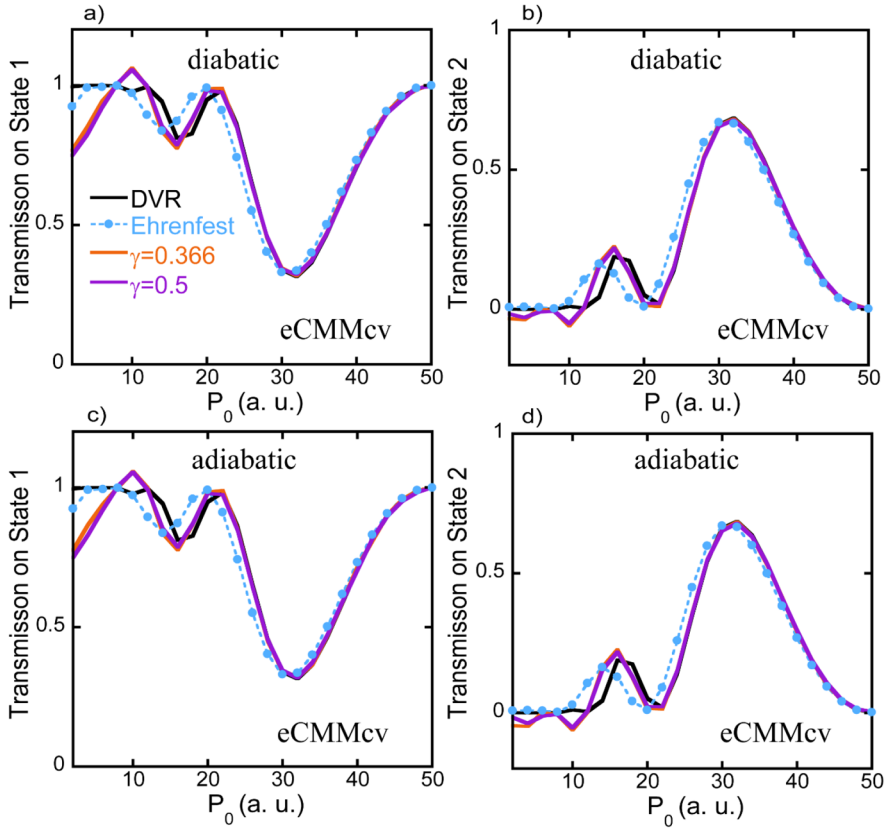

Figure 4. Same as Figure 3, but for transmission coefficients obtained by eCMMcv.

Table 1. Parameters of 3-State Photodissociation Morse Potential Models[58]

parameters	model 1	model 2	model 3
D_1, D_2, D_3	0.003, 0.004, 0.003	0.020, 0.010, 0.003	0.020, 0.020, 0.003
$\beta_1, \beta_2, \beta_3$	0.65, 0.60, 0.65	0.65, 0.40, 0.65	0.40, 0.65, 0.65
R_1, R_2, R_3	5.0, 4.0, 6.0	4.5, 4.0, 4.4	4.0, 4.5, 6.0
C_1, C_2, C_3	0.00, 0.01, 0.006	0.00, 0.01, 0.02	0.02, 0.00, 0.02
A_{12}, A_{23}, A_{31}	0.002, 0.002, 0.0	0.005, 0.0, 0.005	0.005, 0.0, 0.005
R_{12}, R_{23}, R_{31}	3.40, 4.80, 0.00	3.66, 0.00, 3.34	3.40, 0.00, 4.97
$\alpha_{12}, \alpha_{23}, \alpha_{31}$	16.0, 16.0, 0.0	32.0, 0.0, 32.0	32.0, 0.0, 32.0

methods. The models are composed of three Morse potentials with Gaussian coupling terms, which are of the form

$$V_{ii}(x) = D_i[1 - e^{-\beta_i(x-R_i)}]^2 + C_i,\ i = 1, 2, 3.$$
$$V_{ij}(x) = V_{ji}(x) = A_{ij}e^{-\alpha_{ij}(x-R_{ij})^2},\ i, j = 1, 2, 3;\ \text{and}\ i \neq j. \quad (45)$$

The parameters for the three models are listed in Table 1. The nuclear mass is set to $m = 20000$ au. The initial Gaussian wavepacket for the nuclear DOF is prepared from a ground state with frequency $\omega = 5 \times 10^{-3}$ au = 1097 cm^{-1} centering in R_e = 2.9, 3.3, and 2.1 au for models 1, 2, and 3, respectively. The Wigner distribution for the nuclear DOF is

$$\rho(x, p) \propto \exp[-m\omega(x - R_e)^2/\hbar - p^2/(m\omega\hbar)] \quad (46)$$

We use 96 000 trajectories to yield fully converged data in each eCMM or eCMMcv simulation.

The three systems have been studied by a few nonadiabatic dynamics methods based on the Meyer−Miller mapping Hamiltonian.[29,58,90,94] Because the Gaussian coupling terms of eq 45 are relatively local, short-time dynamics implies the Born−Oppenheimer limit.

Figure 5 compares the exact population of each state in each model as a function of time produced by DVR, that generated by eCMM, and that yielded by eCMMcv. While panels a, c, and e demonstrate the eCMM/eCMMcv results with parameter $\gamma = (\sqrt{F+1} - 1)/F = 0.333$ for models 1, 2 and 3, respectively, panels b, d, and f show such results with $\gamma = {}^1/_2$. Figure 5 indicates that eCMMcv is overall superior to eCMM in the three model tests. The eCMMcv approach is more accurate as well as less sensitive to parameter γ. This is mainly because eCMMcv approaches the Born−Oppenheimer limit when the state−state coupling disappears at short times.

In Figure 6, we compare the performance of eCMMcv (with $\gamma = {}^1/_2$ for demonstration) to that of Ehrenfest dynamics. Ehrenfest dynamics produces reasonable short time results but yields significant deviation from the long time limit. In comparison, eCMMcv generates much more accurate results for these three models.

https://doi.org/10.1021/acs.jpca.1c04429
J. Phys. Chem. A 2021, 125, 6845−6863

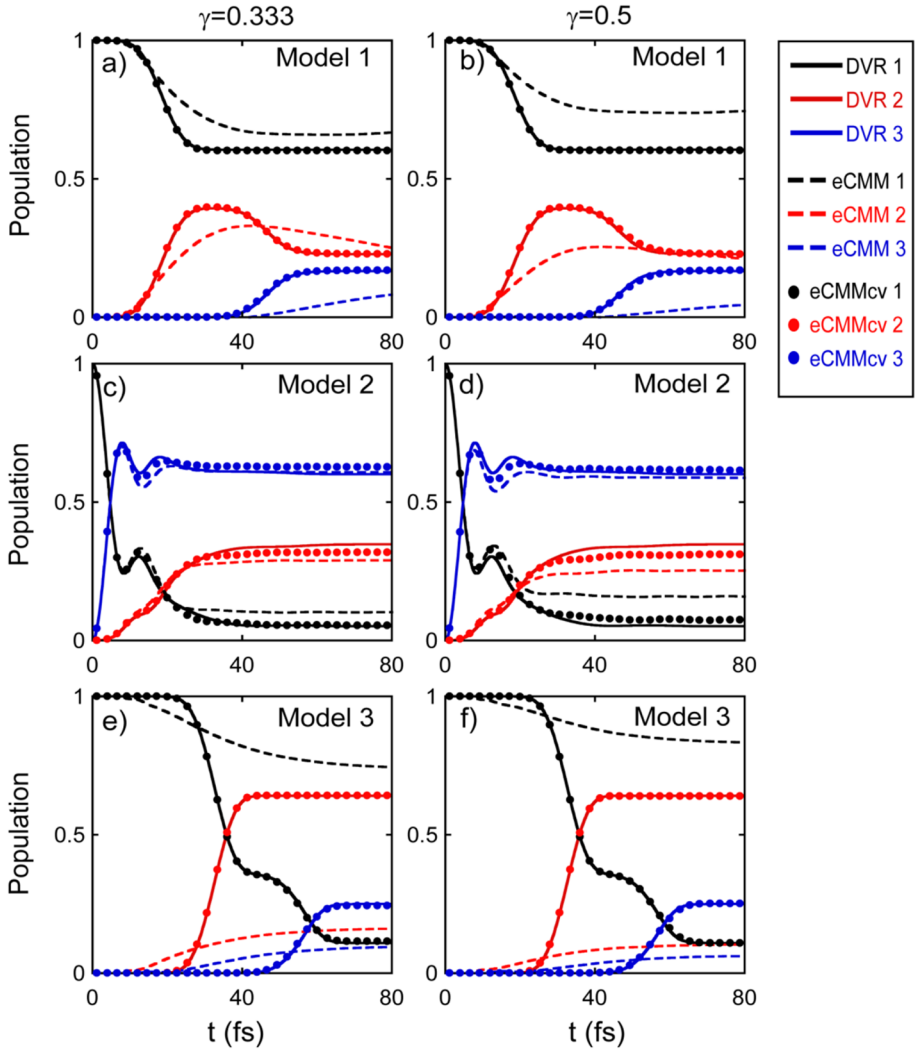

Figure 5. Population dynamics results of the three states for photodissociation models[58] listed in Table 1. The eCMM as well as eCMMcv results are obtained with $\gamma = 0.333$ or $\gamma = 0.5$. Black, red, and blue markers: Populations on state 1, state 2, and state 3, respectively. Solid lines: Exact results produced by DVR. Dashed lines: The eCMM results. Solid circles: The eCMMcv results. Panels a and b are for model 1, panels c and d for model 2, and panels e and f for model 3.

3.3. FMO Monomer. The Fenna−Matthews−Olson (FMO) monomer is a benchmark site-exciton or system−bath model widely used for testing nonadiabatic dynamics methods.[25,28,37,44,46,49,59,97−105] The FMO monomer model includes seven sites, and each site denotes a photosynthetic pigment (Bacteriochlorophyll). The 7-site system is described by the Hamiltonian of ref 59 (in units of wavenumber),

$$H_s = \begin{pmatrix} 12410 & -87.7 & 5.5 & -5.9 & 6.7 & -13.7 & -9.9 \\ -87.7 & 12530 & 30.8 & 8.2 & 0.7 & 11.8 & 4.3 \\ 5.5 & 30.8 & 12210 & -53.5 & -2.2 & -9.6 & 6.0 \\ -5.9 & 8.2 & -53.5 & 12320 & -70.7 & -17.0 & -63.3 \\ 6.7 & 0.7 & -2.2 & -70.7 & 12480 & 81.1 & -1.3 \\ -13.7 & 11.8 & -9.6 & -17.0 & 81.1 & 12630 & 39.7 \\ -9.9 & 4.3 & 6.0 & -63.3 & -1.3 & 39.7 & 12440 \end{pmatrix} \tag{47}$$

and surrounding protein environments are depicted by harmonic baths, $H_b = \sum_{n,i} \frac{1}{2}(P_{ni}^2 + \omega_{ni}^2 R_{ni}^2)$, where $\{R_{ni}, P_{ni}, \omega_{ni}\}$ are the position, momentum, and frequency for the ith bath mode on site n, respectively. Interaction between the system and bath modes adopts a bilinear form, $H_{sb} = -\sum_{n,i} c_{ni} R_{ni} |n\rangle\langle n|$ with c_{ni} being the exciton−phonon or system−bath coupling coefficient, which can be determined from the discretization of the spectral density of the bath. The bath is characterized by a Debye spectral density,[83,106,107] which adopts a Lorentzian cutoff,

$$J(\omega) = 2\lambda \frac{\omega_c \omega}{\omega_c^2 + \omega^2} \tag{48}$$

where λ is the bath reorganization energy and ω_c is the characteristic frequency. A proper discretization scheme is,[108]

$$\begin{cases} \omega_{ni} = \omega_c \tan[\pi/2(1 - i/(1 + N_b))] \\ c_{ni} = \omega_{ni}\sqrt{2\lambda/(1 + N_b)} \end{cases}, \quad i = 1, \cdots, N_b \tag{49}$$

Here N_b is the total number of discretized harmonic modes, and we employ $N_b = 50$ modes per site for converged results. The bath parameters are $\lambda = 35\ \mathrm{cm}^{-1}$, $\omega_c = 106.14\ \mathrm{cm}^{-1}$. We study a relatively low temperature $T = 77\ K$, which is a challenging case for many nonadiabatic dynamics methods. We consider two

https://doi.org/10.1021/acs.jpca.1c04429
J. Phys. Chem. A 2021, 125, 6845−6863

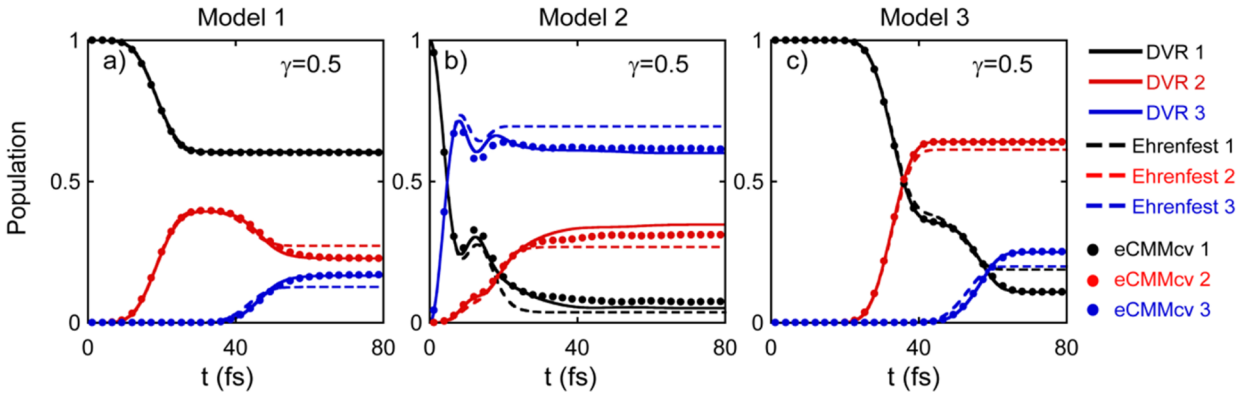

Figure 6. Comparison between eCMMcv and Ehrenfest dynamics. Solid circles: The eCMMcv results with $\gamma = 0.5$. Solid lines: Exact results generated by DVR. Dashed lines: Ehrenfest dynamics. Black, red, and blue colors represent populations on the first, second, and third states, respectively. Panels a, b, and c are for models 1, 2, and 3, respectively.

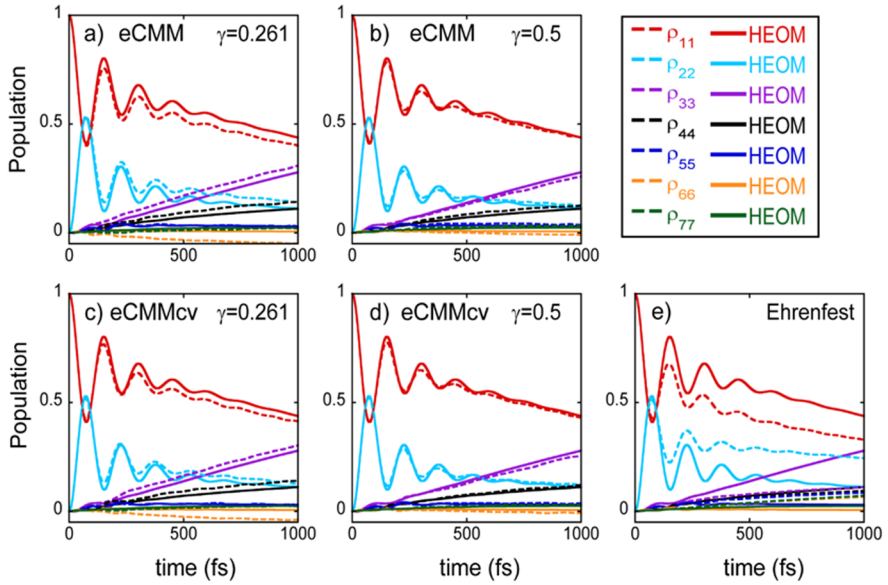

Figure 7. Population dynamics of the 7-state site-exciton model for FMO at 77K, where the initial excitation is on the first pigment (site 1). Panels a and b show the eCMM results with parameter $\gamma = 0.261$ and those with $\gamma = 0.5$, respectively. Red, blue, purple, black, blue, orange, and green lines present populations of sites 1, 2, 3, 4, 5, 6, and 7, respectively. Dashed lines: The eCMM results. Solid lines: Exact results by HEOM. Panels c and d are the same as panels a and b, respectively, but for the eCMMcv results. In panel e, dashed lines are used for Ehrenfest dynamics results, while solid lines are for HEOM results.

different cases. In the first case the initial excitation occurs on pigment/site 1, and in another case pigment/site 6, instead, is excited at the beginning. Since coherence effects could be important in the photoharvesting system, we calculate the population of each site as well as the electronic coherence terms (i.e., the off-diagonal elements of the reduced density matrix for the electronic DOFs). An ensemble of 120 000 trajectories is used in each eCMM or eCMMcv simulation. Several numerically exact approaches are capable of offering benchmark results for the FMO monomer model, which include quasi-adiabatic propagator path integral (QuAPI),[109−111] hierarchical equations of motion (HEOM)[112−120] and multilayer multiconfigurational time-dependent Hartree (ML-MCTDH).[107,121−125] We utilize HEOM to obtain exact results for the FMO model system. Parameter $\gamma = (\sqrt{F+1} - 1)/F \approx 0.261$ or $\gamma = 1/2$ is used for eCMM and eCMMcv.

Figure 7 shows the population of each site of the FMO monomer when site 1 is initially excited. While panels a and b demonstrate the eCMM results for $\gamma = (\sqrt{F+1} - 1)/F \approx 0.261$ and $\gamma = {}^1/_2$, respectively, panels c and d present the corresponding results generated by eCMMcv. Panel e shows that Ehrenfest dynamics works poorly in this case. Figure 8 demonstrates the same information as Figure 7, but for the initial excitation on site 6 instead. It is indicated in Figure 7 and Figure 8 that the results yielded by eCMM are close to those by eCMMcv, which are reasonably accurate in comparison to exact data. The eCMMcv approach performs slightly better than eCMM for this site-exciton model system.

We then study the (electronic) coherence terms. The four most important off-diagonal elements (which have the largest absolute values) of the reduced density matrix are selected for demonstration. The moduli of ρ_{12}, ρ_{13}, ρ_{15}, and ρ_{34} are illustrated in Figure 9 for the case where site 1 is initially excited. When site 6 is excited at the beginning, the moduli of ρ_{34}, ρ_{45}, ρ_{47}, and ρ_{56} are presented in Figure 10. In comparison to the poor performance of Ehrenfest dynamics (as shown in Figure 9e or Figure 10e), either eCMM or eCMMcv yields much more

https://doi.org/10.1021/acs.jpca.1c04429
J. Phys. Chem. A 2021, 125, 6845−6863

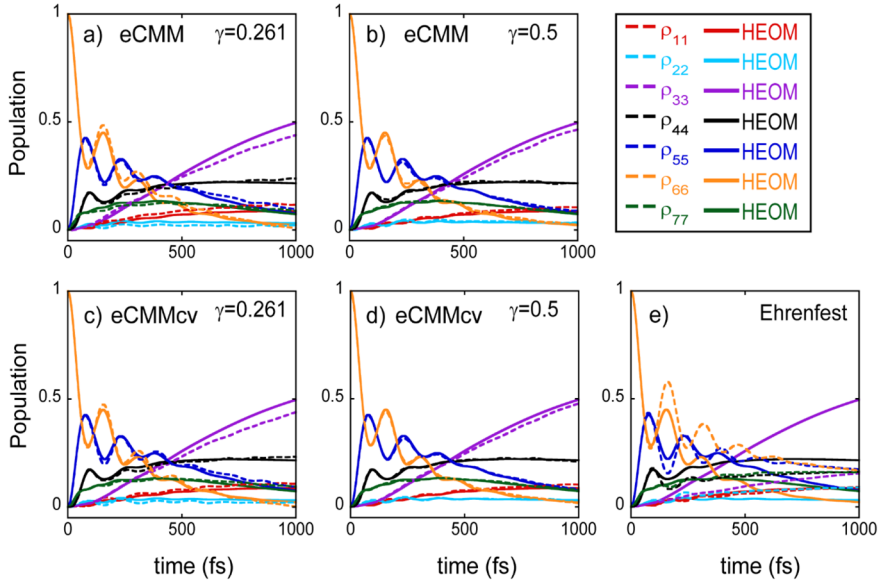

Figure 8. Same as Figure 7, but for the case where the initial excitation occurs on the sixth pigment (site 6).

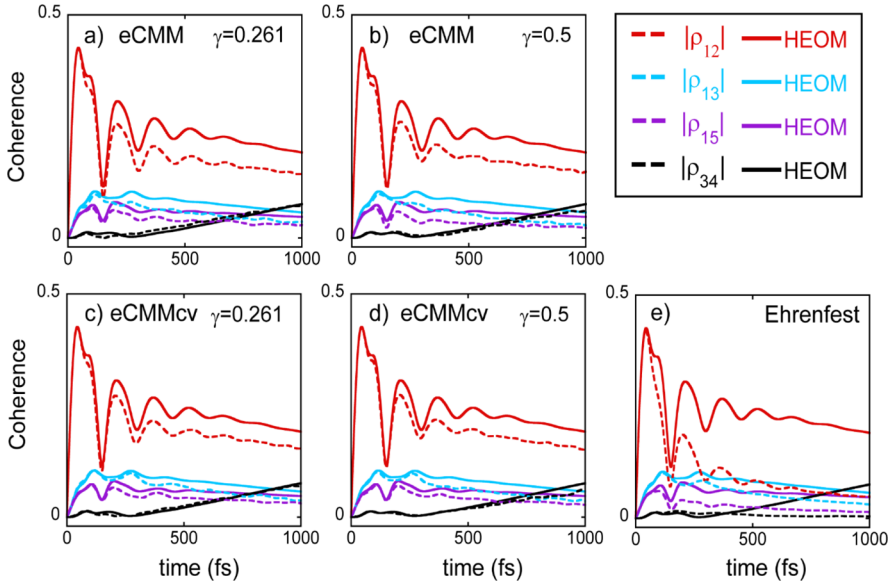

Figure 9. Coherence terms of the 7-state site-exciton model for FMO at 77K, where the initial excitation is on the first pigment (site 1). Panels a and b show the eCMM results with parameter $\gamma = 0.261$ and those with $\gamma = 0.5$, respectively. Red, blue, purple, and and black colors are used for $|\rho_{12}|$, $|\rho_{13}|$, $|\rho_{15}|$, and $|\rho_{34}|$, respectively. Dashed lines: The eCMM results. Solid lines: Exact results by HEOM. Panels c and d are the same as panels a and b, respectively, but for the eCMMcv results. In panel e, dashed lines are used for Ehrenfest dynamics results, while solid lines are for HEOM results.

reasonably good results. The eCMMcv results are slightly closer to the HEOM data than the eCMM ones in Figure 9 and Figure 10.

More results on the population dynamics of each site of the FMO monomer for 77 and 300 K are available in Section S3 of the Supporting Information, in which the eCMM/eCMMcv approaches are compared to Ehrenfest dynamics as well as HEOM. Provided that the eCMM/eCMMcv approaches lead to overall satisfying short-time as well as long-time dynamics results for the FMO monomer for 77 and 300 K, it is reasonable to expect that eCMM/eCMMcv can in principle predict semi-quantitative data for very low temperature or even 0 K, where it is generally difficult for HEOM to obtain converged data. The reliable performance of eCMM for the spin-boson model at 0K has already been demonstrated in refs 41 and 42. Figure 11 compares the population dynamics for site 1 as well as site 3 for the FMO monomer at different temperatures when site 1 is initially activated. As the temperature decreases, the relaxation time scale increases. While the oscillating behavior (of the population dynamics of site 1) vanishes after only two periods (less than 300 fs) at 300 K, such behavior lasts significantly longer than 1000 fs at 0 K as shown in Figure 11.

3.4. Atom-in-Cavity Models. Mixed quantum-classical trajectory-based methods have been utilized to study interaction dynamics of light and matter, which offer approximate but practical approaches for simulating realistic systems in chemistry, materials, and biology.[126−136] We utilize eCMM and eCMMcv to test the performance of describing the cavity-modified chemical dynamics. The benchmark system that we study in this section involves interaction between an atom with

https://doi.org/10.1021/acs.jpca.1c04429
J. Phys. Chem. A 2021, 125, 6845−6863

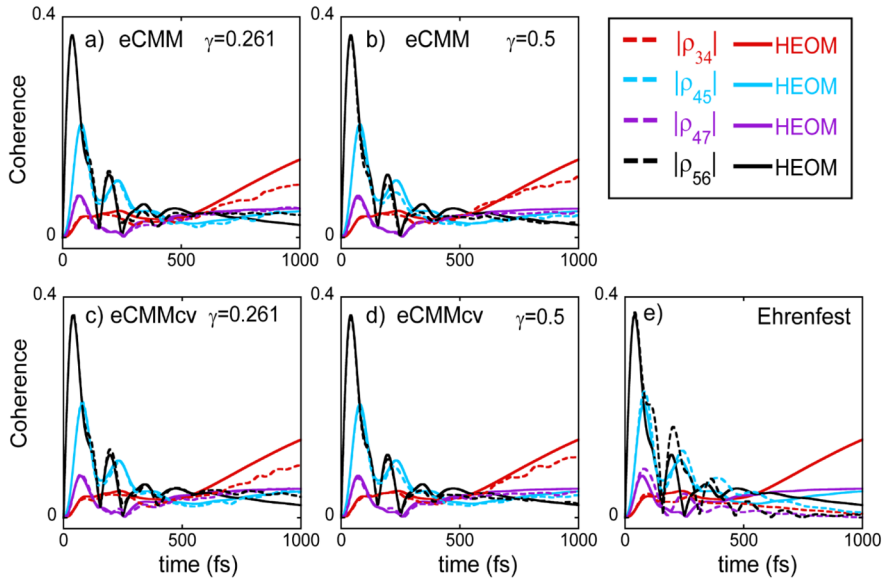

Figure 10. Same as Figure 9, but for the case where the initial excitation occurs on the sixth pigment (site 6). In this case, red, blue, purple, and black lines are used to present $|\rho_{34}|$, $|\rho_{45}|$, $|\rho_{47}|$, and $|\rho_{56}|$, respectively.

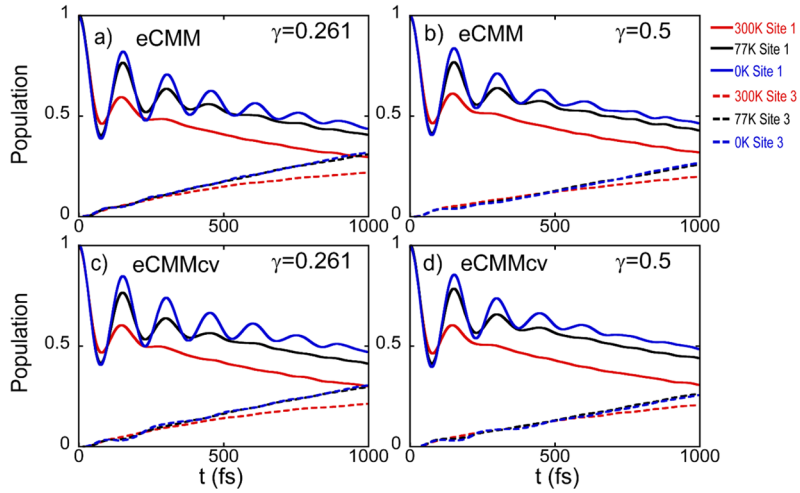

Figure 11. Dynamics at different temperatures for the FMO monomer model when site 1 is initially activated. Red, black, and blue lines represent populations at 300, 77, and 0 K, respectively. Solid lines: The eCMM/eCMMcv results for site 1 (pigment 1). Dashed lines: The eCMM/eCMMcv results for site 3 (pigment 3).

frozen nuclear DOFs in a one-dimmensional lossless cavity, which exhibits relaxation dynamics (for the atom) in conjunction with spontaneous emission of photons.[50,60−63,93,134] The atomic electronic states are coupled because of the interaction of the cavity field and the transition moments between different atomic energy levels. Such a system can be elaborated as a multielectronic-state Hamiltonian model, of which the off-diagonal terms are from the coupling with the cavity field. After making the dipole approximation[137,138] and neglecting the second order interaction (which only leads to a constant shift of the energy level in a two-state system[139]), a general Hamiltonian reads,[62,63]

$$\hat{H} = \sum_{k=1}^{N_e} \varepsilon_k |k\rangle\langle k| + \sum_{k,k'}^{N_e} \sum_{\alpha=1}^{N_p} \omega_\alpha \hat{R}_\alpha \lambda_\alpha \mu_{kk'} |k\rangle\langle k'| + \frac{1}{2} \sum_{\alpha=1}^{N_p} (\hat{P}_\alpha^{\,2} + \omega_\alpha^{\,2} \hat{R}_\alpha^{\,2}) \tag{50}$$

where $|k\rangle$ is the kth atomic energy level, $\{\hat{P}_\alpha, \hat{R}_\alpha, \hat{\omega}_\alpha\}$ denote the momenta, positions, and frequencies of the photonic modes in the cavity, N_e and N_p stand for the number of atomic energy levels and that of cavity field modes, respectively, $\mu_{kk'}$ is the transition dipole moment between two energy levels $|k\rangle$ and $|k'\rangle$, and $\lambda_\alpha \equiv \lambda_\alpha(r_A)$ represents the coupling between the αth field mode and the atom at fixed position r_A. The values of the parameters of the Hamiltonian are given in refs 50, 62, and 63, which we briefly describe below. (All parameters are used in atomic units.)

https://doi.org/10.1021/acs.jpca.1c04429
J. Phys. Chem. A 2021, 125, 6845−6863

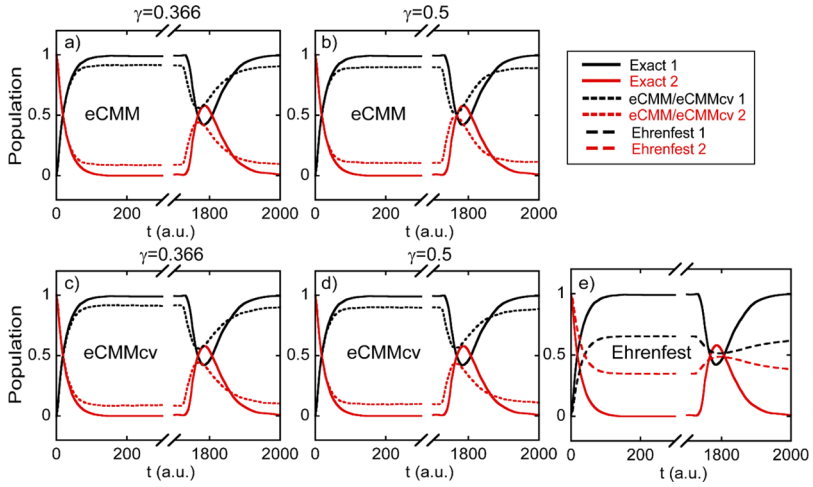

Figure 12. Population as a function of time for the two-level atomic model in optical cavity. Panel a shows the eCMM results with $\gamma = 0.366$, while panel b demonstrates those with $\gamma = 0.5$. Panels c and d are the same as panels a and b, respectively, but for the eCMMcv results. Ehrenfest dynamics results are presented in panel e for comparison. Black color: Population of state 1. Red color: Population of state 2. Solid lines: Exact results from refs 62 and 63. Short-dashed lines: eCMM results in panels a and b or eCMMcv results in panels c and d. Long-dashed lines: Ehrenfest dynamics results in panel e.

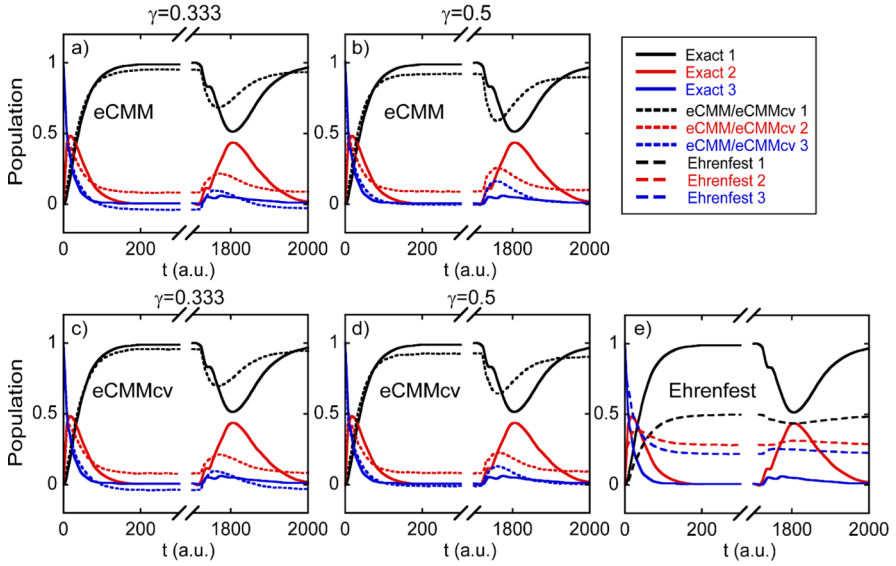

Figure 13. Population as a function of time for the three-level atomic model in optical cavity. Panel a shows the eCMM results with $\gamma = 0.333$, while panel b demonstrates those with $\gamma = 0.5$. Panels c and d are the same as panels a and b, respectively, but for the eCMMcv results. Ehrenfest dynamics results are presented in panel e for comparison. Black, red, and blue colors: Population of state 1, that of state 2, and that of state 3. Solid lines: Exact results from refs 62 and 63. Short-dashed lines: eCMM results in panels a and b, or eCMMcv results in panels c and d. Long-dashed lines: Ehrenfest dynamics results in panel e.

The cavity mode frequencies are determined by the standing-wave condition, i.e.,

$$\omega_\alpha = \frac{\alpha c \pi}{L},\ \alpha = 1, \cdots, N_p \tag{51}$$

here $N_p = 400$ and the coupling vector $\lambda_\alpha(r_A)$ with fixed atom position r_A is

$$\lambda_\alpha(r_A) = \sqrt{\frac{2}{\varepsilon_0 L}}\ \sin\left(\frac{\alpha \pi r_A}{L}\right) \tag{52}$$

where $c = 137.136$ stands for the speed of light, $\varepsilon_0 = 1/(4\pi)$ represents the vacuum permittivity, $L = 2.362 \times 10^5$ is the volume length of the cavity, and the atom is fixed at the center of the cavity $r_A = L/2$. Two models are considered: one is a two-level atom model with atomic energy levels $\varepsilon_1 = -0.6738$ and $\varepsilon_2 = -0.2798$ and transition dipole moment $\mu_{12} = -1.034$; the other is a three-level atom model with atomic energy levels $\varepsilon_1 = -0.6738$, $\varepsilon_2 = -0.2798$, and $\varepsilon_3 = -0.1547$, and transition dipole moments $\mu_{12} = -1.034$ and $\mu_{23} = -2.536$. Four hundred field modes are used in each model. We choose the highest excited state of the atom as the initial state. Each cavity mode is initially in its vacuum state $\langle R_\alpha \mid \Psi_0 \rangle \propto \exp\left[-\omega_\alpha R_\alpha^2/(2\hbar)\right]$ (with zero number of photons). The Wigner distribution of the initial density operator for the cavity field modes then reads

$$\rho_W(\mathbf{R}, \mathbf{P}) \propto \prod_{\alpha=1}^{N_p} \exp[-(P_\alpha^2/(\hbar\omega_\alpha) + \omega_\alpha R_\alpha^2/\hbar)] \tag{53}$$

An ensemble of 96 000 trajectories are used to yield fully converged results for eCMM/eCMMcv. Exact results for the cavity quantum electrodynamics processes in the two models

https://doi.org/10.1021/acs.jpca.1c04429
J. Phys. Chem. A 2021, 125, 6845−6863

can be obtained by the truncated configuration interaction (CI) approach, which are available in refs 62 and 63.

Figure 12 and Figure 13 show the population dynamics of the two-level model and that of the three-level model, respectively. The eCMM and eCMMcv results are obtained with $\gamma = (\sqrt{F+1} - 1)/F = 0.366$ or $\gamma = {}^1/_2$ for the 2-level model, and with $\gamma = (\sqrt{F+1} - 1)/F = 0.333$ or $\gamma = {}^1/_2$ for the 3-level model. The exact data[62,63] and Ehrenfest dynamics results are also demonstrated for comparison. As shown in panel e of Figure 12 and panel e of Figure 13, the Ehrenfest dynamics results considerably deviate from the exact population dynamics even at very short times, which agrees with what was reported in refs 50, 62, and 63. In contrast, Ehrenfest dynamics yields reasonable behavior at very short times in the previous benchmark models studied in the paper, although its long time performance is often poor. This indicates that the atom-in-cavity models are even more challenging for testing the outperformance of a nonadiabatic dynamics method beyond Ehrenfest dynamics. It has been demonstrated in refs 62 and 63 that the fewest switches surface hopping approach[57] generates even worse results than Ehrenfest dynamics.

Figure 12a–d and Figure 13a–d demonstrate that the results yielded by eCMMcv are very similar to those produced by eCMM. Either eCMM or eCMMcv achieves significantly better performance than Ehrenfest dynamics in describing the cavity-modified chemical dynamics of the two models. The reabsorption and re-emission process of the earlier emitted photon by the atom occurs around $t = 1800$ au. It is encouraging that both eCMM and eCMMcv are capable of semiquantitively depicting the positive (negative) spike in the excited (ground) electronic state of the atom. Figures 12 and 13 can be compared to Figures 8 and 12 of ref 63 as well as Figures 1 and 2 of ref 50.

Although eCMMcv is developed in an exact phase space mapping formulation of the correlation function as described in Section 2.1, its trajectory-based dynamics governed by the general mapping Hamiltonian with commutator variables (eq 29 or eq 36) is nevertheless an approximation to the exact equations of motion in quantum mechanics. Although the eCMMcv approach leads to overall reasonably good results in various model tests as shown in Figures 1–13, in the future it will be useful to overcome several drawbacks of eCMMcv. As shown in Figures 3 and 4, neither eCMM nor eCMMcv performs well in the low momentum region, which implies that the performance of eCMMcv should be improved in order to faithfully describe the deep tunneling regime. Figures 3 and 4, Figures 7 and 8, and Figure 13 indicate that negative values for the population of a site/state can occasionally occur in eCMMcv results, while the window function treatment of the SQC approach[29] is expected to solve such a problem. Like most approximate nonadiabatic dynamics methods, the eCMMcv approach does not guarantee that the detail balance is rigorously satisfied for both electronic and nuclear DOFs when the whole system is at thermal equilibrium, although the long time limit results for the electronic DOFs for most model tests are reasonably good. It will be interesting to see how the strategies of refs 140–142 and of refs 143 and 144 can practically be used to systematically improve the mapping Hamiltonian dynamics for multidimensional nonadiabatic systems.

4. CONCLUDING REMARKS

In the conceptually different picture presented in the unified framework for phase space mapping models,[13] it is indicated that there exists a more comprehensive mapping Hamiltonian (eq 29 or eq 36) beyond the well-known Meyer–Miller Hamiltonian[11,12] (eq 3), where commutator matrix $\mathbf{\Gamma}$ that consists of auxiliary mapping variables for $\left\{ -\frac{i}{8}([\hat{\sigma}_x^{(n)}, \hat{\sigma}_y^{(m)}] + [\hat{\sigma}_x^{(m)}, \hat{\sigma}_y^{(n)}]) \right\}$, rather than the conventional zero-point-energy parameter, is involved. In the exact mapping formulation on constraint space for phase space approaches for nonadiabatic dynamics,[41,42] such a general mapping Hamiltonian with commutator variables (eq 29 or eq 36) can be used to produce eCMMcv, an approximate trajectory-based approach. We have tested a few benchmark models that range from gas phase to condensed phase systems, which include the SAC and DAC scattering models,[57] 3-state photodissociation models,[58] 7-site model of the Fenna–Matthews–Olson (FMO) monomer,[59] and atom-in-cavity models.[60−63] Parameter γ in the exact mapping kernel is recommended in the region, $[(\sqrt{F+1} - 1)/F, 1/2]$, where the eCMMcv results are relatively insensitive to the value of γ. The results demonstrate that the overall performance of the general mapping Hamiltonian (eq 29 or eq 36) employed in eCMMcv is better than the original Meyer–Miller Hamiltonian (eq 3) used in eCMM.

The conclusion applies to the most recent version of symmetrical quasi-classical (SQC) dynamics with triangle window functions.[29] The successful SQC methods of Cotton and Miller employ the conventional Meyer–Miller Hamiltonian or its symmetrized form.[18−29] As shown in Section S4 of the Supporting Information, when the original Meyer–Miller Hamiltonian is replaced by the general mapping Hamiltonian with commutator variables (eq 29 or eq 36), the performance of the latest SQC approach of ref 29 can be improved. It is expected that the general mapping Hamiltonian (eq 29 or eq 36) should also be useful in other mixed quantum-classical methods based on the Meyer–Miller mapping Hamiltonian. We note that the additional computation cost for the commutator variables is negligible in comparison to the force for nuclei for realistic systems. So we expect that the general mapping Hamiltonian with commutator variables (eq 29 or eq 36) will be useful for on-the-fly nonadiabatic dynamics.[55,56] (See more discussion for mapping dynamics in the adiabatic representation in Section S1 of the Supporting Information.)

The strategy with a commutator variable matrix can in principle be utilized in other mapping models (e.g., those of the unified framework of ref 13). For example, the general mapping Hamiltonian for Model I of ref 13 in the diabatic representation is

$$H_{map}\left(\mathbf{R}, \mathbf{P}; \mathbf{x}, \mathbf{p}_x, \mathbf{y}, \mathbf{p}_y; \mathbf{\Gamma}\right) = \frac{1}{2}\mathbf{P}^T\mathbf{M}^{-1}\mathbf{P} + \sum_{n,m=1}^{F} [(x^{(n)}p_y^{(m)} - y^{(n)}p_x^{(m)}) - \Gamma_{nm}]V_{mn}(\mathbf{R}) \tag{54}$$

or

https://doi.org/10.1021/acs.jpca.1c04429
J. Phys. Chem. A 2021, 125, 6845−6863

$$H_{map}(\mathbf{R}, \mathbf{P}; \mathbf{x}, \mathbf{p}_x, \mathbf{y}, \mathbf{p}_y; \tilde{\mathbf{x}}, \tilde{\mathbf{p}}) = \frac{1}{2}\mathbf{P}^T\mathbf{M}^{-1}\mathbf{P} + \sum_{n,m=1}^{F} V_{mn}(\mathbf{R})\left[(x^{(n)}p_y^{(m)} - y^{(n)}p_x^{(m)}) - \sum_{k=1}^{F}\frac{s_k}{2}(\tilde{x}_k^{(n)}\tilde{x}_k^{(m)} + \tilde{p}_k^{(n)}\tilde{p}_k^{(m)})\right], \quad (55)$$

where $\{x^{(n)}, y^{(n)}; p_x^{(n)}, p_y^{(n)}\}$ are the mapping variables for the nth electronic DOF. The Hamiltonian with commutator variables of eq 55 should lead to more accurate trajectory-based nonadiabatic dynamics than the mapping Hamiltonian of Model I of ref 13 in the eCMM approach in ref 41 or the SQC approach in ref 145. The isomorphism proposed in ref 146 indicates that either eq 54 or eq 29 is a more general phase space mapping Hamiltonian beyond the conventional Li−Miller Hamiltonian for the second-quantized many-electron Hamiltonian.[147−150] Further investigations along this line will shed light on more comprehensive insight for developing phase space mapping approaches for nonadiabatic dynamic processes from photochemistry to electron transfer, as well as for nonequilibrium electronic transport processes, in realistic experimentally related chemical, biological, and materials systems.[1−10,59,126−136,151−158]

■ ASSOCIATED CONTENT

Supporting Information

The Supporting Information is available free of charge at https://pubs.acs.org/doi/10.1021/acs.jpca.1c04429.

Evolution of nuclear and electronic variables, results for more values for parameter γ in the exact mapping formulation, more results on the FMO monomer, general mapping Hamiltonian with commutator variables in the symmetrical quasi-classical dynamics with triangle window functions, and more simulation details of the eCMM/eCMMcv applications (PDF)

■ AUTHOR INFORMATION

Corresponding Author

Jian Liu − *Beijing National Laboratory for Molecular Sciences, Institute of Theoretical and Computational Chemistry, College of Chemistry and Molecular Engineering, Peking University, Beijing 100871, China;* orcid.org/0000-0002-2906-5858; Email: jianliupku@pku.edu.cn

Authors

Xin He − *Beijing National Laboratory for Molecular Sciences, Institute of Theoretical and Computational Chemistry, College of Chemistry and Molecular Engineering, Peking University, Beijing 100871, China;* orcid.org/0000-0002-5189-7204

Baihua Wu − *Beijing National Laboratory for Molecular Sciences, Institute of Theoretical and Computational Chemistry, College of Chemistry and Molecular Engineering, Peking University, Beijing 100871, China;* orcid.org/0000-0002-1256-6859

Zhihao Gong − *Beijing National Laboratory for Molecular Sciences, Institute of Theoretical and Computational Chemistry, College of Chemistry and Molecular Engineering, Peking University, Beijing 100871, China;* orcid.org/0000-0002-9643-633X

Complete contact information is available at: https://pubs.acs.org/10.1021/acs.jpca.1c04429

Notes

The authors declare no competing financial interest.

■ ACKNOWLEDGMENTS

This work was supported by the National Natural Science Foundation of China (NSFC) Grants No. 21961142017, and by the Ministry of Science and Technology of China (MOST) Grant No. 2017YFA0204901. We acknowledge the High-Performance Computing Platform of Peking University, Beijing PARATERA Tech Co., Ltd., and the Guangzhou supercomputer center for providing computational resources. We thank William H. Miller, Jianshu Cao and Oleg V. Prezhdo for their comments on the manuscript.

■ REFERENCES

(1) Domcke, W.; Yarkony, D. R.; Koppel, H. *Conical Intersections: Theory, Computation and Experiment*. World Scientific: Singapore, 2010.

(2) Martinez, T. J. Seaming Is Believing. *Nature* **2010**, *467*, 412−413.

(3) Long, R.; Prezhdo, O. V.; Fang, W. Nonadiabatic Charge Dynamics in Novel Solar Cell Materials. *Wiley Interdiscip. Rev.: Comput. Mol. Sci.* **2017**, *7*, No. e1305.

(4) Tu, Y.; Zhao, Z.; Lam, J. W. Y.; Tang, B. Z. Mechanistic Connotations of Restriction of Intramolecular Motions (RIM). *Natl. Sci. Rev.* **2021**, *8*, No. nwaa260.

(5) Wang, Y. C.; Ke, Y. L.; Zhao, Y. The Hierarchical and Perturbative Forms of Stochastic Schrodinger Equations and Their Applications to Carrier Dynamics in Organic Materials. *Wiley Interdiscip. Rev. Comput. Mol. Sci.* **2019**, *9*, No. e1375.

(6) Li, W.; Long, R.; Tang, J. F.; Prezhdo, O. V. Influence of Defects on Excited-State Dynamics in Lead Halide Perovskites: Time-Domain Ab Initio Studies. *J. Phys. Chem. Lett.* **2019**, *10*, 3788−3804.

(7) Huang, F.; Bo, Z. S.; Geng, Y. H.; Wang, X. H.; Wang, L. X.; Ma, Y. G.; Hou, J. H.; Hu, W. P.; Pei, J.; Dong, H. L.; et al. Study on Optoelectronic Polymers: An Overview and Outlook. *Acta Polym. Sin.* **2019**, *50*, 988−1046.

(8) Fang, W. H. Ab Initio Determination of Dark Structures in Radiationless Transitions for Aromatic Carbonyl Compounds. *Acc. Chem. Res.* **2008**, *41*, 452−457.

(9) Mai, S. B.; Gonzalez, L. Molecular Photochemistry: Recent Developments in Theory. *Angew. Chem., Int. Ed.* **2020**, *59*, 16832−16846.

(10) Barbatti, M. Photorelaxation Induced by Water-Chromophore Electron Transfer. *J. Am. Chem. Soc.* **2014**, *136*, 10246−10249.

(11) Meyer, H.-D.; Miller, W. H. A Classical Analog for Electronic Degrees of Freedom in Nonadiabatic Collision Processes. *J. Chem. Phys.* **1979**, *70*, 3214−3223.

(12) Stock, G.; Thoss, M. Semiclassical Description of Nonadiabatic Quantum Dynamics. *Phys. Rev. Lett.* **1997**, *78*, 578−581.

(13) Liu, J. A Unified Theoretical Framework for Mapping Models for the Multi-State Hamiltonian. *J. Chem. Phys.* **2016**, *145*, 204105.

(14) Sun, X.; Wang, H. B.; Miller, W. H. Semiclassical Theory of Electronically Nonadiabatic Dynamics: Results of a Linearized Approximation to the Initial Value Representation. *J. Chem. Phys.* **1998**, *109*, 7064−7074.

(15) Coronado, E. A.; Batista, V. S.; Miller, W. H. Nonadiabatic Photodissociation Dynamics of Icn in the (a)over-Tilde Continuum: A Semiclassical Initial Value Representation Study. *J. Chem. Phys.* **2000**, *112*, 5566−5575.

(16) Ananth, N.; Venkataraman, C.; Miller, W. H. Semiclassical Description of Electronically Nonadiabatic Dynamics Via the Initial Value Representation. *J. Chem. Phys.* **2007**, *127*, 084114.

(17) Tao, G.; Miller, W. H. Semiclassical Description of Electronic Excitation Population Transfer in a Model Photosynthetic System. *J. Phys. Chem. Lett.* **2010**, *1*, 891−894.

(18) Cotton, S. J.; Miller, W. H. Symmetrical Windowing for Quantum States in Quasi-Classical Trajectory Simulations: Application to Electronically Non-Adiabatic Processes. *J. Chem. Phys.* **2013**, *139*, 234112.
(19) Cotton, S. J.; Miller, W. H. Symmetrical Windowing for Quantum States in Quasi-Classical Trajectory Simulations. *J. Phys. Chem. A* **2013**, *117*, 7190−7194.
(20) Cotton, S. J.; Igumenshchev, K.; Miller, W. H. Symmetrical Windowing for Quantum States in Quasi-Classical Trajectory Simulations: Application to Electron Transfer. *J. Chem. Phys.* **2014**, *141*, 084104.
(21) Cotton, S. J.; Miller, W. H. A Symmetrical Quasi-Classical Spin-Mapping Model for the Electronic Degrees of Freedom in Non-Adiabatic Processes. *J. Phys. Chem. A* **2015**, *119*, 12138−12145.
(22) Miller, W. H.; Cotton, S. J. Communication: Note on Detailed Balance in Symmetrical Quasi-Classical Models for Electronically Non-Adiabatic Dynamics. *J. Chem. Phys.* **2015**, *142*, 131103.
(23) Miller, W. H.; Cotton, S. J. Communication: Wigner Functions in Action-Angle Variables, Bohr-Sommerfeld Quantization, the Heisenberg Correspondence Principle, and a Symmetrical Quasi-Classical Approach to the Full Electronic Density Matrix. *J. Chem. Phys.* **2016**, *145*, 081102.
(24) Cotton, S. J.; Miller, W. H. A New Symmetrical Quasi-Classical Model for Electronically Non-Adiabatic Processes: Application to the Case of Weak Non-Adiabatic Coupling. *J. Chem. Phys.* **2016**, *145*, 144108.
(25) Cotton, S. J.; Miller, W. H. The Symmetrical Quasi-Classical Model for Electronically Non-Adiabatic Processes Applied to Energy Transfer Dynamics in Site-Exciton Models of Light-Harvesting Complexes. *J. Chem. Theory Comput.* **2016**, *12*, 983−991.
(26) Cotton, S. J.; Liang, R.; Miller, W. H. On the Adiabatic Representation of Meyer−Miller Electronic-Nuclear Dynamics. *J. Chem. Phys.* **2017**, *147*, 064112.
(27) Liang, R. B.; Cotton, S. J.; Binder, R.; Hegger, R.; Burghardt, I.; Miller, W. H. The Symmetrical Quasi-Classical Approach to Electronically Nonadiabatic Dynamics Applied to Ultrafast Exciton Migration Processes in Semiconducting Polymers. *J. Chem. Phys.* **2018**, *149*, 044101.
(28) Cotton, S. J.; Miller, W. H. A Symmetrical Quasi-Classical Windowing Model for the Molecular Dynamics Treatment of Non-Adiabatic Processes Involving Many Electronic States. *J. Chem. Phys.* **2019**, *150*, 104101.
(29) Cotton, S. J.; Miller, W. H. Trajectory-Adjusted Electronic Zero Point Energy in Classical Meyer−Miller Vibronic Dynamics: Symmetrical Quasiclassical Application to Photodissociation. *J. Chem. Phys.* **2019**, *150*, 194110.
(30) Muller, U.; Stock, G. Flow of Zero-Point Energy and Exploration of Phase Space in Classical Simulations of Quantum Relaxation Dynamics. II. Application to Nonadiabatic Processes. *J. Chem. Phys.* **1999**, *111*, 77−88.
(31) Thoss, M.; Stock, G. Mapping Approach to the Semiclassical Description of Nonadiabatic Quantum Dynamics. *Phys. Rev. A: At., Mol., Opt. Phys.* **1999**, *59*, 64−79.
(32) Stock, G.; Thoss, M. Classical Description of Nonadiabatic Quantum Dynamics. *Advances in Chemical Physics* **2005**, *131*, 243−375.
(33) Golosov, A. A.; Reichman, D. R. Classical Mapping Approaches for Nonadiabatic Dynamics: Short Time Analysis. *J. Chem. Phys.* **2001**, *114*, 1065−1074.
(34) Bonella, S.; Coker, D. F. Land-Map, a Linearized Approach to Nonadiabatic Dynamics Using the Mapping Formalism. *J. Chem. Phys.* **2005**, *122*, 194102.
(35) Saller, M. A. C.; Kelly, A.; Richardson, J. O. On the Identity of the Identity Operator in Nonadiabatic Linearized Semiclassical Dynamics. *J. Chem. Phys.* **2019**, *150*, 071101.
(36) Ananth, N.; Miller, T. F. III, Exact Quantum Statistics for Electronically Nonadiabatic Systems Using Continuous Path Variables. *J. Chem. Phys.* **2010**, *133*, 234103.
(37) Huo, P. F.; Coker, D. F. Communication: Partial Linearized Density Matrix Dynamics for Dissipative, Non-Adiabatic Quantum Evolution. *J. Chem. Phys.* **2011**, *135*, 201101.
(38) Huo, P. F.; Coker, D. F. Consistent Schemes for Non-Adiabatic Dynamics Derived from Partial Linearized Density Matrix Propagation. *J. Chem. Phys.* **2012**, *137*, 22A535.
(39) Huo, P. F.; Miller, T. F.; Coker, D. F. Communication: Predictive Partial Linearized Path Integral Simulation of Condensed Phase Electron Transfer Dynamics. *J. Chem. Phys.* **2013**, *139*, 151103.
(40) Kananenka, A. A.; Hsieh, C. Y.; Cao, J. S.; Geva, E. Nonadiabatic Dynamics Via the Symmetrical Quasi-Classical Method in the Presence of Anharmonicity. *J. Phys. Chem. Lett.* **2018**, *9*, 319−326.
(41) He, X.; Liu, J. A New Perspective for Nonadiabatic Dynamics with Phase Space Mapping Models. *J. Chem. Phys.* **2019**, *151*, 024105.
(42) He, X.; Gong, Z.; Wu, B.; Liu, J. Negative Zero-Point-Energy Parameter in the Meyer−Miller Mapping Model for Nonadiabatic Dynamics. *J. Phys. Chem. Lett.* **2021**, *12*, 2496−2501.
(43) Runeson, J. E.; Richardson, J. O. Spin-Mapping Approach for Nonadiabatic Molecular Dynamics. *J. Chem. Phys.* **2019**, *151*, 044119.
(44) Runeson, J. E.; Richardson, J. O. Generalized Spin Mapping for Quantum-Classical Dynamics. *J. Chem. Phys.* **2020**, *152*, 084110.
(45) Liu, Y. D.; Gao, X.; Lai, Y. F.; Mulvihill, E.; Geva, E. Electronic Dynamics through Conical Intersections Via Quasiclassical Mapping Hamiltonian Methods. *J. Chem. Theory Comput.* **2020**, *16*, 4479−4488.
(46) Gao, X.; Geva, E. Improving the Accuracy of Quasiclassical Mapping Hamiltonian Methods by Treating the Window Function Width as an Adjustable Parameter. *J. Phys. Chem. A* **2020**, *124*, 11006−11016.
(47) Gao, X.; Geva, E. A Nonperturbative Methodology for Simulating Multidimensional Spectra of Multiexcitonic Molecular Systems Via Quasiclassical Mapping Hamiltonian Methods. *J. Chem. Theory Comput.* **2020**, *16*, 6491−6502.
(48) Gao, X.; Lai, Y. F.; Geva, E. Simulating Absorption Spectra of Multiexcitonic Systems Via Quasiclassical Mapping Hamiltonian Methods. *J. Chem. Theory Comput.* **2020**, *16*, 6465−6480.
(49) Gao, X.; Saller, M. A. C.; Liu, Y. D.; Kelly, A.; Richardson, J. O.; Geva, E. Benchmarking Quasiclassical Mapping Hamiltonian Methods for Simulating Electronically Nonadiabatic Molecular Dynamics. *J. Chem. Theory Comput.* **2020**, *16*, 2883−2895.
(50) Saller, M. A. C.; Kelly, A.; Geva, E. Benchmarking Quasiclassical Mapping Hamiltonian Methods for Simulating Cavity-Modified Molecular Dynamics. *J. Phys. Chem. Lett.* **2021**, *12*, 3163−3170.
(51) Zheng, J.; Xie, Y.; Jiang, S. S.; Long, Y. Z.; Ning, X.; Lan, Z. G. Ultrafast Electron Transfer with Symmetrical Quasi-Classical Dynamics Based on Mapping Hamiltonian and Quantum Dynamics Based on Ml-Mctdh. *Chin. J. Chem. Phys.* **2017**, *30*, 800−810.
(52) Xie, Y.; Zheng, J.; Lan, Z. G. Performance Evaluation of the Symmetrical Quasi-Classical Dynamics Method Based on Meyer−Miller Mapping Hamiltonian in the Treatment of Site-Exciton Models. *J. Chem. Phys.* **2018**, *149*, 174105.
(53) Zheng, J.; Peng, J. W.; Xie, Y.; Long, Y. Z.; Ning, X.; Lan, Z. G. Study of the Exciton Dynamics in Perylene Bisimide (Pbi) Aggregates with Symmetrical Quasiclassical Dynamics Based on the Meyer−Miller Mapping Hamiltonian. *Phys. Chem. Chem. Phys.* **2020**, *22*, 18192−18204.
(54) Peng, J. W.; Xie, Y.; Hu, D. P.; Lan, Z. G. Analysis of Bath Motion in Mm-Sqc Dynamics Via Dimensionality Reduction Approach: Principal Component Analysis. *J. Chem. Phys.* **2021**, *154*, 094122.
(55) Tang, D. D.; Fang, W. H.; Shen, L.; Cui, G. L. Combining Meyer−Miller Hamiltonian with Electronic Structure Methods for on-the-Fly Nonadiabatic Dynamics Simulations: Implementation and Application. *Phys. Chem. Chem. Phys.* **2019**, *21*, 17109−17117.
(56) Hu, D. P.; Xie, Y.; Peng, J. W.; Lan, Z. G. On-the-Fly Symmetrical Quasi-Classical Dynamics with Meyer−Miller Mapping Hamiltonian for the Treatment of Nonadiabatic Dynamics at Conical Intersections. *J. Chem. Theory Comput.* **2021**, *17*, 3267−3279.
(57) Tully, J. C. Molecular-Dynamics with Electronic-Transitions. *J. Chem. Phys.* **1990**, *93*, 1061−1071.

https://doi.org/10.1021/acs.jpca.1c04429
J. Phys. Chem. A 2021, 125, 6845−6863

(58) Coronado, E. A.; Xing, J. H.; Miller, W. H. Ultrafast Non-Adiabatic Dynamics of Systems with Multiple Surface Crossings: A Test of the Meyer−Miller Hamiltonian with Semiclassical Initial Value Representation Methods. *Chem. Phys. Lett.* **2001**, *349*, 521−529.
(59) Ishizaki, A.; Fleming, G. R. Theoretical Examination of Quantum Coherence in a Photosynthetic System at Physiological Temperature. *Proc. Natl. Acad. Sci. U. S. A.* **2009**, *106*, 17255−17260.
(60) Su, Q.; Eberly, J. H. Model Atom for Multiphoton Physics. *Phys. Rev. A: At., Mol., Opt. Phys.* **1991**, *44*, 5997−6008.
(61) Flick, J.; Ruggenthaler, M.; Appel, H.; Rubio, A. Atoms and Molecules in Cavities, from Weak to Strong Coupling in Quantum-Electrodynamics (QED) Chemistry. *Proc. Natl. Acad. Sci. U. S. A.* **2017**, *114*, 3026−3034.
(62) Hoffmann, N. M.; Schafer, C.; Rubio, A.; Kelly, A.; Appel, H. Capturing Vacuum Fluctuations and Photon Correlations in Cavity Quantum Electrodynamics with Multitrajectory Ehrenfest Dynamics. *Phys. Rev. A: At., Mol., Opt. Phys.* **2019**, *99*, 063819.
(63) Hoffmann, N. M.; Schafer, C.; Sakkinen, N.; Rubio, A.; Appel, H.; Kelly, A. Benchmarking Semiclassical and Perturbative Methods for Real-Time Simulations of Cavity-Bound Emission and Interference. *J. Chem. Phys.* **2019**, *151*, 244113.
(64) Wigner, E. On the Quantum Correction for Thermodynamic Equilibrium. *Phys. Rev.* **1932**, *40*, 749−759.
(65) Wigner, E. P. *Perspectives in Quantum Theory*; MIT: Cambridge, MA, 1971.
(66) Born, M.; Jordan, P. On Quantum Mechanics. *Eur. Phys. J. A* **1925**, *34*, 858−888.
(67) Kirkwood, J. G. Quantum Statistics of Almost Classical Assemblies. *Phys. Rev.* **1933**, *44*, 31.
(68) Husimi, K. Some Formal Properties of the Density Matrix. *Proc. Phys. Math. Soc. Jpn.* **1940**, *22*, 264−314.
(69) Rivier, D. C. On a One-to-One Correspondence between Infinitesimal Canonical Transformations and Infinitesimal Unitary Transformations. *Phys. Rev.* **1951**, *83*, 862.
(70) Margenau, H.; Hill, R. N. Correlation between Measurements in Quantum Theory. *Prog. Theor. Phys.* **1961**, *26*, 722−738.
(71) Sudarshan, E. C. G. Equivalence of Semiclassical and Quantum Mechanical Descriptions of Statistical Light Beams. *Phys. Rev. Lett.* **1963**, *10*, 277.
(72) Mehta, C. L. Phase-Space Formulation of Dynamics of Canonical Variables. *J. Math. Phys.* **1964**, *5*, 677.
(73) Glauber, R. J. Coherent and Incoherent States of Radiation Field. *Phys. Rev.* **1963**, *131*, 2766.
(74) Glauber, R. J. *Quantum Optics and Electronics*; Gordon and Breach: New York, 1965.
(75) Rihaczek, A. W. Signal Energy Distribution in Time and Frequency. *IEEE Trans. Inf. Theory* **1968**, *14*, 369.
(76) Drummond, P. D.; Gardiner, C. W. Generalized P-Representations in Quantum Optics. *J. Phys. A: Math. Gen.* **1980**, *13*, 2353−2368.
(77) Cohen, L.; Zaparovanny, Y. I. Positive Quantum Joint Distributions. *J. Math. Phys.* **1980**, *21*, 794−796.
(78) Kruger, J. In *Second International Wigner Symposium*; Goslar, Germany, 1991.
(79) Cohen, L. Generalized Phase-Space Distribution Functions. *J. Math. Phys.* **1966**, *7*, 781.
(80) Lee, H. W. Theory and Application of the Quantum Phase-Space Distribution-Functions. *Phys. Rep.* **1995**, *259*, 147−211.
(81) Liu, J.; Miller, W. H. An Approach for Generating Trajectory-Based Dynamics Which Conserves the Canonical Distribution in the Phase Space Formulation of Quantum Mechanics. I. Theories. *J. Chem. Phys.* **2011**, *134*, 104101.
(82) Liu, J.; Miller, W. H. An Approach for Generating Trajectory-Based Dynamics Which Conserves the Canonical Distribution in the Phase Space Formulation of Quantum Mechanics. II. Thermal Correlation Functions. *J. Chem. Phys.* **2011**, *134*, 104102.
(83) Wang, H. B.; Song, X. Y.; Chandler, D.; Miller, W. H. Semiclassical Study of Electronically Nonadiabatic Dynamics in the Condensed-Phase: Spin-Boson Problem with Debye Spectral Density. *J. Chem. Phys.* **1999**, *110*, 4828−4840.
(84) Kim, H.; Nassimi, A.; Kapral, R. Quantum-Classical Liouville Dynamics in the Mapping Basis. *J. Chem. Phys.* **2008**, *129*, 084102.
(85) Nassimi, A.; Bonella, S.; Kapral, R. Analysis of the Quantum-Classical Liouville Equation in the Mapping Basis. *J. Chem. Phys.* **2010**, *133*, 134115.
(86) Kelly, A.; van Zon, R.; Schofield, J.; Kapral, R. Mapping Quantum-Classical Liouville Equation: Projectors and Trajectories. *J. Chem. Phys.* **2012**, *136*, 084101.
(87) Wang, H.; Sun, X.; Miller, W. H. Semiclassical Approximations for the Calculation of Thermal Rate Constants for Chemical Reactions in Complex Molecular Systems. *J. Chem. Phys.* **1998**, *108*, 9726−9736.
(88) Shi, Q.; Geva, E. A Relationship between Semiclassical and Centroid Correlation Functions. *J. Chem. Phys.* **2003**, *118*, 8173.
(89) Bonella, S.; Coker, D. F. Semiclassical Implementation of the Mapping Hamiltonian Approach for Nonadiabatic Dynamics Using Focused Initial Distribution Sampling. *J. Chem. Phys.* **2003**, *118*, 4370−4385.
(90) Huo, P. F.; Coker, D. F. Semi-Classical Path Integral Non-Adiabatic Dynamics: A Partial Linearized Classical Mapping Hamiltonian Approach. *Mol. Phys.* **2012**, *110*, 1035−1052.
(91) Leggett, A. J.; Chakravarty, S.; Dorsey, A. T.; Fisher, M. P. A.; Garg, A.; Zwerger, M. Dynamics of the Dissipative Two-State System. *Rev. Mod. Phys.* **1987**, *59*, 1−85.
(92) Fenna, R. E.; Matthews, B. W. Chlorophyll Arrangement in a Bacteriochlorophyll Protein from Chlorobium-Limicola. *Nature* **1975**, *258*, 573−577.
(93) Buzek, V.; Drobny, G.; Kim, E. G.; Havukainen, M.; Knight, P. L. Numerical Simulations of Atomic Decay in Cavities and Material Media. *Phys. Rev. A: At., Mol., Opt. Phys.* **1999**, *60*, 582−592.
(94) Tao, G. H. Coherence-Controlled Nonadiabatic Dynamics Via State-Space Decomposition: A Consistent Way to Incorporate Ehrenfest and Born-Oppenheimer-Like Treatments of Nuclear Motion. *J. Phys. Chem. Lett.* **2016**, *7*, 4335−4339.
(95) Colbert, D. T.; Miller, W. H. A Novel Discrete Variable Representation for Quantum-Mechanical Reactive Scattering Via the S-Matrix Kohn Method. *J. Chem. Phys.* **1992**, *96*, 1982−1991.
(96) Ibele, L. M.; Curchod, B. F. E. A Molecular Perspective on Tully Models for Nonadiabatic Dynamics. *Phys. Chem. Chem. Phys.* **2020**, *22*, 15183−15196.
(97) Saller, M. A. C.; Kelly, A.; Richardson, J. O. Improved Population Operators for Multi-State Nonadiabatic Dynamics with the Mixed Quantum-Classical Mapping Approach. *Faraday Discuss.* **2020**, *221*, 150−167.
(98) Tao, G. H.; Miller, W. H. Semiclassical Description of Electronic Excitation Population Transfer in a Model Photosynthetic System. *J. Phys. Chem. Lett.* **2010**, *1*, 891−894.
(99) Tao, G. H.; Shen, N. Mapping State Space to Quasiclassical Trajectory Dynamics in Coherence-Controlled Nonadiabatic Simulations for Condensed Phase Problems. *J. Phys. Chem. A* **2017**, *121*, 1734−1748.
(100) Wu, J. L.; Liu, F.; Shen, Y.; Cao, J. S.; Silbey, R. J. Efficient Energy Transfer in Light-Harvesting Systems, I: Optimal Temperature, Reorganization Energy and Spatial-Temporal Correlations. *New J. Phys.* **2010**, *12*, 105012.
(101) Moix, J.; Wu, J. L.; Huo, P. F.; Coker, D.; Cao, J. S. Efficient Energy Transfer in Light-Harvesting Systems, III: The Influence of the Eighth Bacteriochlorophyll on the Dynamics and Efficiency in Fmo. *J. Phys. Chem. Lett.* **2011**, *2*, 3045−3052.
(102) Wu, J. L.; Liu, F.; Ma, J.; Silbey, R. J.; Cao, J. S. Efficient Energy Transfer in Light-Harvesting Systems: Quantum-Classical Comparison, Flux Network, and Robustness Analysis. *J. Chem. Phys.* **2012**, *137*, 174111.
(103) Cao, J. S.; Cogdell, R. J.; Coker, D. F.; Duan, H. G.; Hauer, J.; Kleinekathofer, U.; Jansen, T. L. C.; Mancal, T.; Miller, R. J. D.; Ogilvie, J. P.; et al. Quantum Biology Revisited. *Sci. Adv.* **2020**, *6*, No. eaaz4888.

https://doi.org/10.1021/acs.jpca.1c04429
J. Phys. Chem. A 2021, 125, 6845−6863

(104) Tang, Z. F.; Gong, Z. H.; Wu, J. L. Generalized Quantum Kinetic Expansion: Time Scale Separation between Intra-Cluster and Inter-Cluster Kinetics. *J. Chem. Phys.* **2015**, *143*, 104107.
(105) Wu, J. L.; Tang, Z. F.; Gong, Z. H.; Cao, J. S.; Mukamel, S. Minimal Model of Quantum Kinetic Clusters for the Energy-Transfer Network of a Light-Harvesting Protein Complex. *J. Phys. Chem. Lett.* **2015**, *6*, 1240−1245.
(106) Garg, A.; Onuchic, J. N.; Ambegaokar, V. Effect of Friction on Electron-Transfer in Biomolecules. *J. Chem. Phys.* **1985**, *83*, 4491−4503.
(107) Thoss, M.; Wang, H. B.; Miller, W. H. Self-Consistent Hybrid Approach for Complex Systems: Application to the Spin-Boson Model with Debye Spectral Density. *J. Chem. Phys.* **2001**, *115*, 2991−3005.
(108) Craig, I. R.; Thoss, M.; Wang, H. Proton Transfer Reactions in Model Condensed-Phase Environments: Accurate Quantum Dynamics Using the Multilayer Multiconfiguration Time-Dependent Hartree Approach. *J. Chem. Phys.* **2007**, *127*, 144503.
(109) Makarov, D. E.; Makri, N. Path-Integrals for Dissipative Systems by Tensor Multiplication - Condensed-Phase Quantum Dynamics for Arbitrarily Long-Time. *Chem. Phys. Lett.* **1994**, *221*, 482−491.
(110) Makri, N.; Makarov, D. E. Tensor Propagator for Iterative Quantum Time Evolution of Reduced Density-Matrices.2. Numerical Methodology. *J. Chem. Phys.* **1995**, *102*, 4611−4618.
(111) Topaler, M.; Makri, N. Path Integral Calculation of Quantum Nonadiabatic Rates in Model Condensed Phase Reactions. *J. Phys. Chem.* **1996**, *100*, 4430−4436.
(112) Tanimura, Y.; Kubo, R. Time Evolution of a Quantum System in Contact with a Nearly Gaussian-Markoffian Noise Bath. *J. Phys. Soc. Jpn.* **1989**, *58*, 101−114.
(113) Yan, Y. A.; Yang, F.; Liu, Y.; Shao, J. S. Hierarchical Approach Based on Stochastic Decoupling to Dissipative Systems. *Chem. Phys. Lett.* **2004**, *395*, 216−221.
(114) Xu, R. X.; Cui, P.; Li, X. Q.; Mo, Y.; Yan, Y. J. Exact Quantum Master Equation Via the Calculus on Path Integrals. *J. Chem. Phys.* **2005**, *122*, 041103.
(115) Shao, J. S. Stochastic Description of Quantum Open Systems: Formal Solution and Strong Dissipation Limit. *Chem. Phys.* **2006**, *322*, 187−192.
(116) Moix, J. M.; Cao, J. S. A Hybrid Stochastic Hierarchy Equations of Motion Approach to Treat the Low Temperature Dynamics of Non-Markovian Open Quantum Systems. *J. Chem. Phys.* **2013**, *139*, 134106.
(117) Tanimura, Y. Reduced Hierarchical Equations of Motion in Real and Imaginary Time: Correlated Initial States and Thermodynamic Quantities. *J. Chem. Phys.* **2014**, *141*, 044114.
(118) Tanimura, Y. Real-Time and Imaginary-Time Quantum Hierarchal Fokker-Planck Equations. *J. Chem. Phys.* **2015**, *142*, 144110.
(119) Yan, Y. J. Theory of Open Quantum Systems with Bath of Electrons and Phonons and Spins: Many-Dissipaton Density Matrixes Approach. *J. Chem. Phys.* **2014**, *140*, 054105.
(120) Hsieh, C. Y.; Cao, J. S. A Unified Stochastic Formulation of Dissipative Quantum Dynamics. I. Generalized Hierarchical Equations. *J. Chem. Phys.* **2018**, *148*, 014103.
(121) Wang, H. B.; Thoss, M.; Miller, W. H. Systematic Convergence in the Dynamical Hybrid Approach for Complex Systems: A Numerically Exact Methodology. *J. Chem. Phys.* **2001**, *115*, 2979−2990.
(122) Wang, H. B.; Thoss, M. Multilayer Formulation of the Multiconfiguration Time-Dependent Hartree Theory. *J. Chem. Phys.* **2003**, *119*, 1289−1299.
(123) Wang, H. B.; Thoss, M. From Coherent Motion to Localization: Dynamics of the Spin-Boson Model at Zero Temperature. *New J. Phys.* **2008**, *10*, 115005.
(124) Worth, G. A.; Meyer, H. D.; Koppel, H.; Cederbaum, L. S.; Burghardt, I. Using the Mctdh Wavepacket Propagation Method to Describe Multimode Non-Adiabatic Dynamics. *Int. Rev. Phys. Chem.* **2008**, *27*, 569−606.
(125) Wang, H. B.; Thoss, M. From Coherent Motion to Localization: II. Dynamics of the Spin-Boson Model with Sub-Ohmic Spectral Density at Zero Temperature. *Chem. Phys.* **2010**, *370*, 78−86.
(126) Chen, H. T.; Li, T. E.; Sukharev, M.; Nitzan, A.; Subotnik, J. E. Ehrenfest Plus R Dynamics. I. A Mixed Quantum-Classical Electrodynamics Simulation of Spontaneous Emission. *J. Chem. Phys.* **2019**, *150*, 044102.
(127) Li, T. E.; Chen, H. T.; Subotnik, J. E. Comparison of Different Classical, Semiclassical, and Quantum Treatments of Light-Matter Interactions: Understanding Energy Conservation. *J. Chem. Theory Comput.* **2019**, *15*, 1957−1973.
(128) Mandal, A.; Krauss, T. D.; Huo, P. F. Polariton-Mediated Electron Transfer Via Cavity Quantum Electrodynamics. *J. Phys. Chem. B* **2020**, *124*, 6321−6340.
(129) Chen, H. T.; Li, T. E.; Nitzan, A.; Subotnik, J. E. Predictive Semiclassical Model for Coherent and Incoherent Emission in the Strong Field Regime: The Mollow Triplet Revisited. *J. Phys. Chem. Lett.* **2019**, *10*, 1331−1336.
(130) Li, T. E.; Chen, H. T.; Nitzan, A.; Sukharev, M.; Subotnik, J. E. A Necessary Trade-Off for Semiclassical Electrodynamics: Accurate Short-Range Coulomb Interactions Versus the Enforcement of Causality? *J. Phys. Chem. Lett.* **2018**, *9*, 5955−5961.
(131) Mandal, A.; Montillo Vega, S.; Huo, P. F. Polarized Fock States and the Dynamical Casimir Effect in Molecular Cavity Quantum Electrodynamics. *J. Phys. Chem. Lett.* **2020**, *11*, 9215−9223.
(132) Li, X. Y.; Mandal, A.; Huo, P. F. Cavity Frequency-Dependent Theory for Vibrational Polariton Chemistry. *Nat. Commun.* **2021**, *12*, 1315.
(133) Li, T. E.; Chen, H. T.; Nitzan, A.; Subotnik, J. E. Understanding the Nature of Mean-Field Semiclassical Light-Matter Dynamics: An Investigation of Energy Transfer, Electron-Electron Correlations, External Driving, and Long-Time Detailed Balance. *Phys. Rev. A: At., Mol., Opt. Phys.* **2019**, *100*, 062509.
(134) Li, T. E.; Chen, H. T.; Nitzan, A.; Subotnik, J. E. Quasiclassical Modeling of Cavity Quantum Electrodynamics. *Phys. Rev. A: At., Mol., Opt. Phys.* **2020**, *101*, 033831.
(135) Li, T. E.; Nitzan, A.; Sukharev, M.; Martinez, T.; Chen, H. T.; Subotnik, J. E. Mixed Quantum-Classical Electrodynamics: Understanding Spontaneous Decay and Zero-Point Energy. *Phys. Rev. A: At., Mol., Opt. Phys.* **2018**, *97*, 032105.
(136) Li, T. E.; Subotnik, J. E.; Nitzan, A. Cavity Molecular Dynamics Simulations of Liquid Water under Vibrational Ultrastrong Coupling. *Proc. Natl. Acad. Sci. U. S. A.* **2020**, *117*, 18324−18331.
(137) Meystre, P.; Sargent, M. *Elements of Quantum Optics*; Springer-Verlag: Berlin, 2007.
(138) Ruggenthaler, M.; Tancogne-Dejean, N.; Flick, J.; Appel, H.; Rubio, A. From a Quantum-Electrodynamical Light-Matter Description to Novel Spectroscopies. *Nat. Rev. Chem.* **2018**, *2*, 390−391.
(139) Schafer, C.; Ruggenthaler, M.; Rubio, A. Ab Initio Nonrelativistic Quantum Electrodynamics: Bridging Quantum Chemistry and Quantum Optics from Weak to Strong Coupling. *Phys. Rev. A: At., Mol., Opt. Phys.* **2018**, *98*, 043801.
(140) Moix, J.; Pollak, E.; Shao, J. Generalized Liouville Time-Dependent Perturbation Theory. *Phys. Rev. A: At., Mol., Opt. Phys.* **2009**, *80*, 052103.
(141) Liu, X.; Zhang, L.; Liu, J. Machine Learning Phase Space Quantum Dynamics Approaches. *J. Chem. Phys.* **2021**, *154*, 184104.
(142) Filinov, V. S.; Medvedev, Y. V.; Kamskyi, V. L. Quantum Dynamics and Wigner Representation of Quantum Mechanics. *Mol. Phys.* **1995**, *85*, 711−726.
(143) Kryvohuz, M.; Cao, J. S. Quantum-Classical Correspondence in Response Theory. *Phys. Rev. Lett.* **2005**, *95*, 180405.
(144) Kryvohuz, M.; Cao, J. S. Classical Divergence of Nonlinear Response Functions. *Phys. Rev. Lett.* **2006**, *96*, 030403.
(145) Zheng, J.; Xie, Y.; Jiang, S. S.; Long, Y. Z.; Ning, X.; Lan, Z. G. Initial Sampling in Symmetrical Quasiclassical Dynamics Based on Li-Miller Mapping Hamiltonian. *Phys. Chem. Chem. Phys.* **2019**, *21*, 26502−26514.
(146) Liu, J. Isomorphism between the Multi-State Hamiltonian and the Second-Quantized Many-Electron Hamiltonian with Only 1-Electron Interactions. *J. Chem. Phys.* **2017**, *146*, 024110.

https://doi.org/10.1021/acs.jpca.1c04429
J. Phys. Chem. A 2021, 125, 6845−6863

(147) Li, B.; Miller, W. H. A Cartesian Classical Second-Quantized Many-Electron Hamiltonian, for Use with the Semiclassical Initial Value Representation. *J. Chem. Phys.* **2012**, *137*, 154107.
(148) Li, B.; Levy, T. J.; Swenson, D. W. H.; Rabani, E.; Miller, W. H. A Cartesian Quasi-Classical Model to Nonequilibrium Quantum Transport: The Anderson Impurity Model. *J. Chem. Phys.* **2013**, *138*, 104110.
(149) Li, B.; Miller, W. H.; Levy, T. J.; Rabani, E. Classical Mapping for Hubbard Operators: Application to the Double-Anderson Model. *J. Chem. Phys.* **2014**, *140*, 204106.
(150) Li, B.; Wilner, E. Y.; Thoss, M.; Rabani, E.; Miller, W. H. A Quasi-Classical Mapping Approach to Vibrationally Coupled Electron Transport in Molecular Junctions. *J. Chem. Phys.* **2014**, *140*, 104110.
(151) Feng, S. S.; Wang, Y. C.; Ke, Y. L.; Liang, W. Z.; Zhao, Y. Effect of Charge-Transfer States on the Vibrationally Resolved Absorption Spectra and Exciton Dynamics in Znpc Aggregates: Simulations from a Non-Makovian Stochastic Schrodinger Equation. *J. Chem. Phys.* **2020**, *153*, 034116.
(152) Feng, S.; Wang, Y.-C.; Liang, W.; Zhao, Y. Vibrationally Resolved Absorption Spectra and Exciton Dynamics in Zinc Phthalocyanine Aggregates: Effects of Aggregation Lengths and Remote Exciton Transfer. *J. Phys. Chem. A* **2021**, *125*, 2932−2943.
(153) Tatchen, J.; Pollak, E. Ab Initio Spectroscopy and Photo-induced Cooling of the Trans-Stilbene Molecule. *J. Chem. Phys.* **2008**, *128*, 164303.
(154) Sisto, A.; Glowacki, D. R.; Martinez, T. J. Ab Initio Nonadiabatic Dynamics of Multichromophore Complexes: A Scalable Graphical-Processing-Unit-Accelerated Exciton Framework. *Acc. Chem. Res.* **2014**, *47*, 2857−2866.
(155) Peng, Q.; Ma, H. L.; Shuai, Z. G. Theory of Long-Lived Room-Temperature Phosphorescence in Organic Aggregates. *Acc. Chem. Res.* **2021**, *54*, 940−949.
(156) Wang, Y. C.; Feng, S. S.; Liang, W. Z.; Zhao, Y. Electronic Couplings for Photoinduced Charge Transfer and Excitation Energy Transfer Based on Fragment Particle-Hole Densities. *J. Phys. Chem. Lett.* **2021**, *12*, 1032−1039.
(157) Zobel, J. P.; Bokareva, O. S.; Zimmer, P.; Wolper, C.; Bauer, M.; Gonzalez, L. Intersystem Crossing and Triplet Dynamics in an Iron(II) N-Heterocyclic Carbene Photosensitizer. *Inorg. Chem.* **2020**, *59*, 14666−14678.
(158) Nijjar, P.; Jankowska, J.; Prezhdo, O. V. Ehrenfest and Classical Path Dynamics with Decoherence and Detail Balance. *J. Chem. Phys.* **2019**, *150*, 204124.

https://doi.org/10.1021/acs.jpca.1c04429
J. Phys. Chem. A 2021, 125, 6845−6863